ARTICLES

# Mechanism of shape determination in motile cells

Kinneret Keren[1,3]*, Zachary Pincus[1,4]*, Greg M. Allen[1], Erin L. Barnhart[1], Gerard Marriott[5], Alex Mogilner[6] & Julie A. Theriot[1,2]

**The shape of motile cells is determined by many dynamic processes spanning several orders of magnitude in space and time, from local polymerization of actin monomers at subsecond timescales to global, cell-scale geometry that may persist for hours. Understanding the mechanism of shape determination in cells has proved to be extremely challenging due to the numerous components involved and the complexity of their interactions. Here we harness the natural phenotypic variability in a large population of motile epithelial keratocytes from fish (*Hypsophrys nicaraguensis*) to reveal mechanisms of shape determination. We find that the cells inhabit a low-dimensional, highly correlated spectrum of possible functional states. We further show that a model of actin network treadmilling in an inextensible membrane bag can quantitatively recapitulate this spectrum and predict both cell shape and speed. Our model provides a simple biochemical and biophysical basis for the observed morphology and behaviour of motile cells.**

Cell shape emerges from the interaction of many constituent elements—notably, the cytoskeleton, the cell membrane and cell–substrate adhesions—that have been studied in great detail at the molecular level[1–3]; however, the mechanism by which global morphology is generated and maintained at the cellular scale is not understood. Many studies have characterized the morphological effects of perturbing various cytoskeletal and other cellular components (for example, ref. 4); yet, there have been no comprehensive efforts to try to understand cell shape from first principles. Here we address this issue in the context of motile epithelial keratocytes derived from fish skin. Fish keratocytes are among the fastest moving animal cells, and their motility machinery is characterized by extremely rapid molecular dynamics and turnover[5–8]. At the same time, keratocytes are able to maintain nearly constant speed and direction during movement over many cell lengths. Their shapes, consisting of a bulbous cell body at the rear attached to a broad, thin lamellipodium at the front and sides, are simple, stereotyped and notoriously temporally persistent[9,10]. The molecular dynamism of these cells, combined with the persistence of their global shape and behaviour, make them an ideal model system for investigating the mechanisms of cell shape determination.

The relative simplicity of keratocytes has inspired extensive experimental and theoretical investigations into this cell type[5–17], considerably advancing the understanding of cell motility. A notable example is the graded radial extension (GRE) model[12], which was an early attempt to link the mechanism of motility at the molecular level with overall cell geometry. The GRE model proposed that local cell extension (either protrusion or retraction) occurs perpendicular to the cell edge, and that the magnitude of this extension is graded from a maximum near the cell midline to a minimum towards the sides. Although this phenomenological model has been shown experimentally to describe keratocyte motion, it does not consider what generates the graded extension rates, neither does it explain what determines the cellular geometry in the first place. Thus, even for these simple cells, it has remained unclear how the biochemical and biophysical molecular dynamics underlying motility give rise to large-scale cell geometry. In this work we address this question by exploiting the natural phenotypic variability in keratocytes to measure the relations among cell geometry, actin distribution and motility. On the basis of quantitative observations of a large number of cells, we have developed a model that relates overall cell geometry to the dynamics of actin network treadmilling and the forces imposed on this network by the cell membrane. This model is able to quantitatively explain the main features of keratocyte shapes and to predict the relationship between cell geometry and speed.

## Low-dimensional keratocyte shape space

Individual keratocytes assume a variety of cell shapes (Fig. 1a). A quantitative characterization[18,19] of a large population of live keratocytes revealed that keratocyte shapes are well described with just four orthogonal modes of shape variability (Fig. 1b), which together account for ~97% of the total variation in shape. Roughly, these modes can be characterized as measures of: the projected cell area (mode 1); whether the cell has a rounded 'D' shape or an elongated 'canoe' shape (mode 2)[11]; the angle of the rear of the lamellipodium with respect to the cell body (mode 3); and the left–right asymmetry of the side lobes (mode 4). These shape modes provide a meaningful and concise quantitative description of keratocyte morphology using very few parameters. Specifically, over 93% of the cell-to-cell shape variation can be captured by recording only two parameters per cell: the cell's position along shape modes 1 and 2, or, essentially equivalently, its projected area and aspect ratio. Two additional parameters are required to describe the detailed shape of the rear of the cell (shape modes 3 and 4). The existence of only a few meaningful modes implies that the phase space in which keratocytes reside is a relatively small subregion of the space of all possible shapes.

To investigate further the role of various molecular processes in determining cell shape, we targeted specific components of the

[1]Department of Biochemistry, and [2]Department of Microbiology and Immunology, Stanford University School of Medicine, Stanford, California 94305, USA. [3]Department of Physics, Technion- Israel Institute of Technology, Haifa 32000, Israel. [4]Department of Molecular, Cellular and Developmental Biology, Yale University, New Haven, Connecticut 06520, USA. [5]Department of Physiology, University of Wisconsin at Madison, Madison, Wisconsin 53706, USA. [6]Department of Neurobiology, Physiology and Behavior and Department of Mathematics, University of California, Davis, California 95616, USA.
*These authors contributed equally to this work.

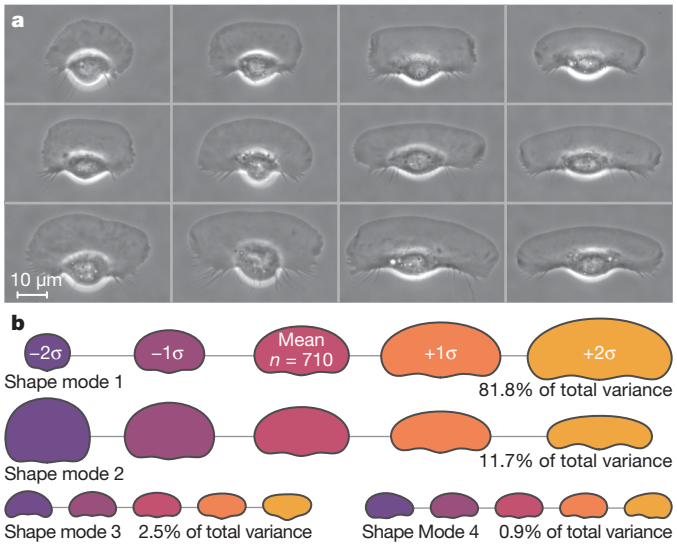


**Figure 1 | Keratocyte shapes are described by four primary shape modes.** **a**, Phase-contrast images of different live keratocytes illustrate the natural shape variation in the population. **b**, The first four principal modes of keratocyte shape variation, as determined by principal components analysis of 710 aligned outlines of live keratocytes, are shown. These modes—cell area (shape mode 1), 'D' versus 'canoe' shape (shape mode 2), cell-body position (shape mode 3), and left–right asymmetry (shape mode 4)—are highly reproducible; subsequent modes seem to be noise. For each mode, the mean cell shape is shown alongside reconstructions of shapes one and two standard deviations away from the mean in each direction along the given mode. The variation accounted for by each mode is indicated. (Modes one and two are scaled as in **a**; modes three and four are 50% smaller.)

cytoskeleton in live cells with pharmacological agents that affect actin dynamics or myosin activity. The different treatments elicited statistically significant morphological changes (Supplementary Fig. 1), but their extent was rather small. In particular, the natural shape variation in the population (Fig. 1) was substantially larger than the shifts induced by any of the perturbations (Supplementary Fig. 1). Furthermore, whereas the shape of an individual cell can be significantly affected by such perturbations[11], the phase space of cell shapes under the perturbations tested was nearly identical to that spanned by the population of unperturbed cells (Supplementary Fig. 1). This led us to focus on the phenotypic variability in unperturbed populations, which, as described, provided significant insight into the underlying mechanisms of shape determination.

## Cell shape is dynamically determined

The natural phenotypic variability described presents a spectrum of possible functional states of the system. To better characterize these states, we measured cell speed, area, aspect ratio and other morphological features in a large number of live cells (Fig. 2a) and correlated these traits across the population (Fig. 2b; see also the Supplementary Information). To relate these measures to cellular actin dynamics, we concurrently examined the distribution of actin filaments along the leading edge. To visualize actin filaments in live cells, we used low levels of tetramethylrhodamine (TMR)-derivatized kabiramide C, which at low concentrations binds as a complex with G-actin to free barbed ends of actin filaments[20,21], so that along the leading edge the measured fluorescence intensity is proportional to the local density of filaments.

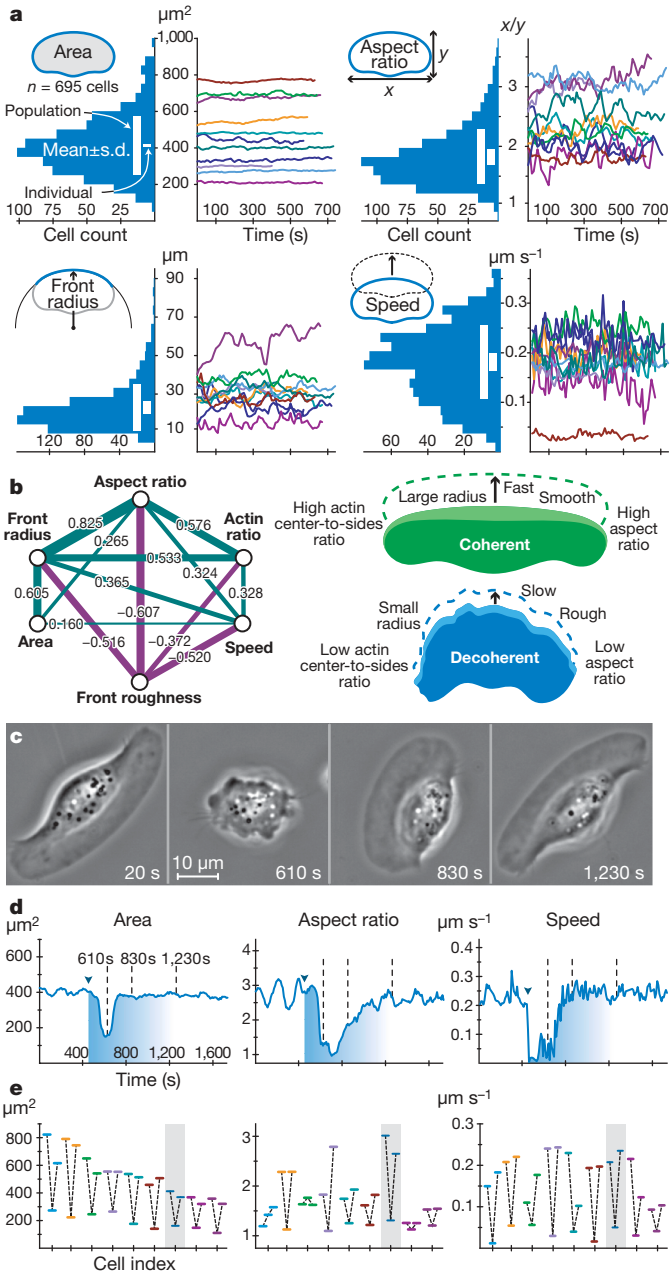


**Figure 2 | Quantitative and correlative analysis of keratocyte morphology and speed.** **a**, The distributions of measures across a population of live keratocytes (left panels) are contrasted with values through time for 11 individual cells (right). Within each histogram, the population mean ± one standard deviation is shown by the left vertical bar, whereas the population mean ± the average standard deviation exhibited by individual cells over 5 min is shown by the right bar. **b**, Significant pair-wise correlations ($P < 0.05$; bootstrap confidence intervals) within a population of keratocytes are diagrammed (left panel). Two additional measures are included: front roughness, which measures the local irregularity of the leading edge, and actin ratio, which represents the peakedness of the actin distribution along the leading edge. The correlations indicate that, apart from size differences, cells lie along a single phenotypic continuum (right panel), from 'decoherent' to 'coherent'. Decoherent cells move slowly and assume rounded shapes with low aspect ratios and high lamellipodial curvatures. The actin network is less ordered, with ragged leading edges and low actin ratios. Coherent cells move faster and have lower lamellipodial curvature. The actin network is highly ordered with smooth leading edges and high actin ratios. **c**, Phase-contrast images depict a cell transiently treated with DMSO (Supplementary Movie 1), which caused a reversible inhibition of motility and loss of the lamellipodium. Images shown correspond to before (20 s), during (610 s) and two time points after (830 s and 1,230 s) the perturbation. **d**, Time traces of area, aspect ratio and speed for the cell in **c** show that shape and speed are regained post perturbation. Dashed lines show time points from **c**; arrowheads indicate the time of perturbation. **e**, Area, aspect ratio and speed of nine cells are shown as averages obtained from one-minute windows before, during and after DMSO treatment (shown sequentially from left to right for each cell). The cell shown in **c** and **d** is highlighted.

The phenotypic variability in our test population is depicted in the histograms shown in Fig. 2a. We further characterized this variability by following several individual cells over time. Particularly notable was the observation that the projected cell area, although quite variable across the population, was essentially constant for a given cell (Fig. 2a). This suggests that the area, probably determined by the total amount of available plasma membrane or by tight regulation of the membrane surface area, is intrinsic to each cell and constant through time. Individual cells showed larger variability in other measures such as speed and aspect ratio; nevertheless, in every case, individual variability remained smaller than that of the population as a whole (Fig. 2a). The measured properties correlate well across the data set (Fig. 2b and Supplementary Fig. 2), producing a phenotypic continuum that we have described previously[11]: from rough, slow and rounded 'decoherent' cells, to smooth, fast and wide 'coherent' cells that exhibit a more pronounced peak in actin filament density at the centre.

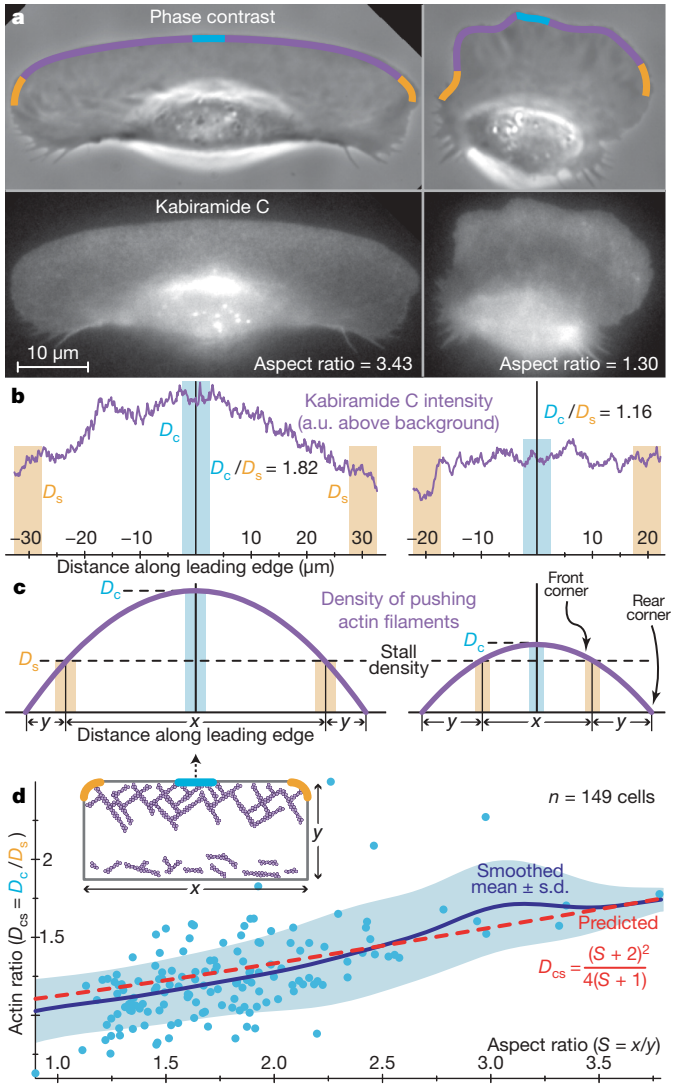


**Figure 3 | A quantitative model explains the main features of keratocyte shapes. a**, Phase-contrast (top) and fluorescence (bottom) images are shown for two live keratocytes stained with TMR-derivatized kabiramide C. The fluorescence intensity reflects the current and past distribution of filament ends, in addition to diffuse background signal from unincorporated probe[20]. Along the leading edge, the fluorescence intensity is proportional to the local density of actin filaments (see Supplementary Information; 1-μm-wide strips along the leading edge are shown superimposed on the phase-contrast images, with centre and side regions highlighted). **b**, The average (background-corrected) fluorescence intensity along the strips shown in **a** is plotted. The cell on the left has a peaked distribution of actin filaments, whereas the actin distribution in the cell on the right is flatter. The ratio of the actin density at the centre ($D_c$) and sides ($D_s$; averaged over both sides) of the strip, denoted as $D_{cs}$, serves as a robust measure of the peakedness of the distribution. **c**, The density distribution of pushing actin filaments along the leading edge is approximated as a parabola, with a maximum at the centre. Cells with peaked filamentous actin distributions and, therefore, high $D_{cs}$ values, have larger regions in which the actin filament density is above the 'stall' threshold, and thus have longer protruding front edges (of length $x$) compared with the length of the stalled/retracting cell sides ($y$), yielding higher aspect ratios ($S = x/y$). **d**, The ratio between actin density at the centre and at the sides, $D_{cs}$, is plotted as a function of cell aspect ratio, $S$. Each data point represents an individual cell. Our model provides a parameter-free prediction of this relationship (red line), which captures the mean trend in the data, plotted as a gaussian-weighted moving average ($\sigma = 0.25$; blue line) ± one standard deviation (blue region). Inset: the model of cell shape is illustrated schematically.

To examine the role that the particular history of a given cell has in determining cell morphology, we confronted keratocytes with an acute perturbation—transient treatment with high concentrations of dimethylsulphoxide (DMSO)—which resulted in temporary lamellipodial loss and cell rounding[22]. We found that cells were able to resume movement (albeit in an arbitrary direction with respect to their orientation before DMSO treatment) and return to their original morphology and speed within minutes (Fig. 2c–e), comparable to the characteristic timescales of the underlying molecular processes such as actin assembly and disassembly and adhesion formation[5–8,23]. This rapid recovery of pre-perturbation properties suggests that the observed, persistent behaviour of keratocytes is a manifestation of a dynamic system at steady state. Taken together, our results imply that cell shape and speed are determined by a history-independent self-organizing mechanism, characterized by a small number of cellular parameters that stay essentially constant over time (such as available quantities of membrane or cytoskeletal components), independent of the precise initial localization of the components of the motility machinery.

## Actin/membrane model explains cell shape

We set out to develop a quantitative physical model of cell shape and movement that could explain this observed spectrum of keratocyte behaviour. Specifically, we sought to describe mechanistically the shape variability captured in the first two principal modes of keratocyte shape (Fig. 1b; comprising over 93% of the total shape variation), setting aside the detailed shape of the cell rear. Two observations—first, that cell area is constant (Fig. 2a), and second, that the density of filamentous actin along the leading edge is graded (Fig. 3a,b)—are central to our proposed mechanism of cell shape regulation. In addition, this mechanism is predicated on the basis of previous observations that the lamellipodial actin network undergoes treadmilling, with net assembly at the leading edge and net disassembly towards the rear[8,24,25].

We hypothesize that actin polymerization pushes the cell membrane from within, generating membrane tension[26]. The cell membrane, which has been observed to remain nearly stationary in the cell frame of reference in keratocytes[12,14], is fluid and bends easily but is nevertheless inextensible (that is, it can be deformed but not stretched)[27]. Forces on the membrane at any point equilibrate within milliseconds[26] (see Supplementary Information) so that, on the timescales relevant for motility, membrane tension is spatially homogenous at all points along the cell boundary. At the leading edge, membrane tension imposes an opposing force on growing actin filaments that is constant per unit edge length, so that the force per filament is inversely proportional to the local filament density. At the centre of the leading edge, where filament density is high (Fig. 3a–c), the membrane resistance per filament is small, allowing filaments to grow rapidly and generate protrusion. As filament density gradually decreases towards the cell sides, the forces per filament caused by membrane tension increase until polymerization is stalled at the far sides of the cell, which therefore neither protrude nor retract. At the rear of the cell, where the actin network disassembles,

membrane tension, assisted by myosin contraction, crushes the weakened network and moves actin debris forward, thereby retracting the cell rear (Fig. 3d, inset). Membrane tension, which is spatially constant, thus induces a direct coupling between molecular processes occurring at distant regions of the cell and contributes to the global coordination of those processes. The Supplementary Information discusses alternative hypotheses regarding cell shape determination that are inconsistent with our measurements (Supplementary Fig. 3).

This qualitative model can be mathematically specified and quantitatively compared to our data set as follows (see Supplementary Table 1 for a list of model assumptions, and Supplementary Information for further details). As discussed previously (Fig. 1), keratocyte shapes can largely be described by two parameters: shape modes 1 and 2, which essentially correspond to cell area ($A$) and aspect ratio ($S$), respectively. Thus, for simplicity, we begin by approximating cells as rectangles with width $x$ and length $y$ ($A = xy$, $S = x/y$, and the total leading edge length (front and sides) is $L = x + 2y = \sqrt{AS} + 2\sqrt{A/S}$). The observed steady-state centre-peaked distribution of actin filaments along the leading edge ($D$) can be described as a parabola: $D(l) = \frac{\beta}{L\gamma}\left(1 - \left(\frac{l}{L/2}\right)^2\right)$, where $l$ is the arc distance along the leading edge ($l = 0$ at the cell midline), $\beta$ is the total number of nascent actin filaments that branch off from existing growing filaments per cell per second, and $\gamma$ is the rate of capping of existing filaments (Fig. 3c; see Supplementary Information for derivation). We make the further assumption (described previously) that actin filament protrusion is mechanically stalled by the membrane tension $T$ at the sides of the front of the lamellipodium ($l = \pm x/2$). The force acting on each filament at the sides must therefore be approximately equal to the force required to stall a single actin filament[28], $f_{\mathrm{stall}}$, which has been measured[29,30], so that: $D_s = D(x/2) = \frac{\beta}{L\gamma}\left(1 - \left(\frac{x}{L}\right)^2\right) = \frac{T}{f_{\mathrm{stall}}}$. We find that the peak actin density $D_c = D(0)$ fluctuates more than $D_s$ across the population and in individual cells through time (Supplementary Fig. 4; Supplementary Information), suggesting that most of the shape variation observed correlates with differences in actin dynamics rather than changes in membrane tension.

This simple model provides a direct link between the distribution of filamentous actin and overall cell morphology. From the previous equations, this link can be expressed as a relation between the ratio of actin filament density at the centre ($l = 0$) versus the sides ($l = \pm x/2$) of the leading edge, denoted $D_{cs}$, and the aspect ratio of the cell, $S$: $D_{cs} = \frac{D_c}{D_s} = \left[1 - \left(\frac{x}{L}\right)^2\right]^{-1} = \frac{(S+2)^2}{4(S+1)}$. Thus, cells with relatively more actin filament density at the centre than the sides (high $D_{cs}$) have higher aspect ratios, whereas cells with low $D_{cs}$ ratios have aspect ratios closer to one. As shown in Fig. 3d, the correlation between $D_{cs}$ and $S$ in our measurements closely follows this model prediction, which, importantly, involves no free parameters. The model is further supported by perturbation experiments, in which, for example, increasing the capping rate $\gamma$ (by treatment with cytochalasin D) led to the predicted decrease in cell aspect ratio (Supplementary Fig. 1; Supplementary Information). Remarkably, all the model parameters apart from area can be combined into a single parameter: $z = \frac{T\gamma}{f_{\mathrm{stall}}\beta}$, which signifies the ratio of the membrane tension to the force needed to stall actin network growth at the centre of the leading edge. This key parameter can be expressed in multiple ways: $z \equiv \frac{T\gamma}{f_{\mathrm{stall}}\beta} = \frac{1}{L}\left(1 - \left(\frac{x}{L}\right)^2\right) = \frac{1}{L \cdot D_{cs}}$; that is, in terms of the membrane tension, filament stall force, and branching and capping rates; in terms of the measurable geometry of the cell alone; or in terms of the actin density ratio and cell geometry (see also Supplementary Fig. 5). Thus, this model describes the basic relation between actin network dynamics at the molecular level and overall actin network structure and shape at the cellular scale using only two biologically relevant parameters: $z$ and $A$.

## Shape, speed and lamellipodial radius

To describe cell shape with more accuracy and to relate cell speed to morphology, we must consider the relationship between the growth rate of actin filaments and the magnitude of force resisting their growth. This so-called force–velocity relationship can be used to determine the protrusion rate at the leading edge, and thus cell speed, from the forces exerted by the membrane against the growing lamellipodial actin network. Because membrane tension is the same everywhere along the leading edge, although the filamentous actin density is peaked at the centre of the leading edge, the resistive force per filament increases with distance from the centre. As a result, local protrusion rates decrease smoothly from the centre towards the sides of the leading edge (where, as above, protrusion is stalled). Assuming that protrusion is locally perpendicular to the cell boundary, this implies that the sides of the leading edge lag behind the centre, causing the leading edge to become curved as observed (Fig. 1a; such a relation between geometry and spatially variable protrusion rates was first described in the GRE model[12]). Thus, keratocytes can be more accurately described as slightly bent rectangles, characterized by the radius of curvature of their leading edge, $R$, and their overall rate of movement (Fig. 4), in addition to their width and length.

Given a particular force–velocity relation, both cell speed and lamellipodial radius can be expressed, in the context of this model, solely in terms of the parameters $A$ and $z$. Thus, speed and radius are predicted to vary with cell area and aspect ratio, providing further tests of the model. The exact form of the force–velocity relation for the lamellipodial actin network is unknown. Measurements in branched actin networks, both in motile keratocytes[16] and assembled in cytoplasmic extracts[31], yielded force–velocity relations that were concave down: that is, the protrusion rate was insensitive to force at weak loads (relative to the stall force), whereas at greater loads the speed decreased markedly. Regardless of its precise functional dependence, as long as the force–velocity relation entails such a monotonic concave-down decrease in protrusion velocity with increasing membrane tension, the predicted trends in cell speed and lamellipodium radius correlate well with our experimental observations (Supplementary Fig. 6). We find good quantitative agreement between the model and our observations using a force–velocity relation given by $V = V_0\left(1 - \left(\frac{f}{f_{\mathrm{stall}}}\right)^w\right)$, where $w = 8$ (Fig. 4).

By combining this force–velocity relation with the geometric formulae of the GRE model, we obtain $R \approx \frac{L}{8}\sqrt{(zL)^{-8} - 1}$ (see Supplementary

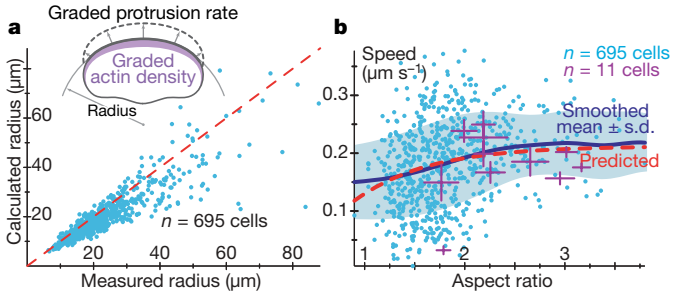


**Figure 4 | An extended model predicts lamellipodial curvature and the relationship between speed and morphology.** **a**, The radius of curvature of the leading edge calculated within the model as a function of $A$ and $S$, $R_c = \frac{L}{8}\sqrt{(zL)^{-8} - 1}$, with $zL = \frac{4(S+1)}{(S+2)^2}$ and $L = \sqrt{AS} + 2\sqrt{A/S}$, is plotted against the measured radius of curvature ($R_m$, radius of best-fit circle of the front 40% of the cell). The red dashed line depicts $R_c = R_m$. **b**, Cell speed, $V_{\mathrm{cell}}$, is shown as a function of cell aspect ratio, $S$. The model prediction $V_{\mathrm{cell}} = V_0\left(1 - \left(\frac{4(S+1)}{(S+2)^2}\right)^8\right)$ (red line; $V_0$ determined empirically) is compared to the trend plotted as a gaussian-weighted moving average ($\sigma = 0.25$; blue line) ± one standard deviation (blue region), from 695 individual cells (blue points). Purple crosses indicate the mean ± one standard deviation in speed and aspect ratio over 5 min for 11 individual cells (shown in Fig. 2a).

Information), which predicts the radius of curvature of a cell's leading edge from its area and aspect ratio alone. Figure 4a demonstrates the close agreement between the measured and the calculated radii of curvature. At the centre of the leading edge, $f = T/D_c$; therefore, $V_{cell} = V_0\left(1-\left(\frac{T}{f_{stall}D_c}\right)^8\right) = V_0\left(1-(zL)^8\right) = V_0\left(1-\left(\frac{4(S+1)}{(S+2)^2}\right)^8\right)$. Thus, a cell's speed can be predicted from its aspect ratio, with more canoe-like cells expected to move faster. We find that the trend of the experimental data agrees with our predictions (Fig. 4b), and, in particular, shows the predicted saturation of speed with increasing aspect ratio. We expect cell-to-cell variation in some of the model parameters that determine cell speed such as the concentration of actin monomers and the fraction of pushing actin filaments, as well as in the rate of retrograde actin flow with respect to the substrate[13,17]. Without detailed per-cell measurements of these, we use constant values that reflect the population mean, allowing correct prediction of population trends, whereas some aspects of cell-to-cell variation remain unexplained.

## Discussion

We have used correlative approaches to map quantitatively the functional states of keratocyte motility from a large number of observations of morphology, speed and actin network structure in a population of cells. This data set provided the basis for and constraints on a quantitative model of cell shape that requires only two cell-dependent parameters; these parameters are measurable from cell geometry alone and are closely related to the two dimensions of a phase space that accounts for over 93% of all keratocyte shape variation. Although conceptually quite straightforward, our model describes connections between dynamic events spanning several orders of magnitude in space and time and is, to our knowledge, the first quantitative approach relating molecular mechanisms to cell geometry and movement. The model is able to explain specific properties of keratocyte shape and locomotion on the basis of a coupling of tension in the cell membrane to the dynamics of the treadmilling network of actin filaments. Overall, the picture is very simple: actin network treadmilling (characterized by the $z$ parameter) drives from within the forward protrusion of an inextensible membrane bag (characterized in two dimensions by its total area). Such a scenario was suggested over a decade ago[32], but prior to this work had never been tested. Furthermore, this basic mechanism seems to be sufficient to explain the persistent and coordinated movement of keratocytes without incorporating regulatory elements such as microtubules, morphogens or signalling molecules[33], suggesting that, at least in keratocytes, these elements are dispensable or redundant.

The model highlights the important regulatory role of membrane tension in cell shape determination: actin assembly at the leading edge and disassembly at the cell rear are both modulated by forces imposed on the actin network by the membrane. Moreover, because membrane tension is constant along the cell boundary, it effectively couples processes (such as protrusion and retraction) that take place in spatially distinct regions of the cell. On the basis of our results, we estimate the membrane tension in motile keratocytes to be on the order of 100 pN $\mu m^{-1}$ (see Supplementary Information), similar to the results of experiments that estimated membrane tension from the force on a tether pulled from the surface of motile fibroblasts[34].

Our model does not specifically address adhesion or the detailed shape of the cell rear (captured in shape modes 3 and 4; Fig. 1b). Nevertheless, adhesive contacts to the substrate are obviously essential for the cell to be able to generate traction and to move forward. We assume implicitly that the lamellipodial actin network is attached to the substrate, which allows polymerization to translate into cellular protrusion. This assumption is consistent with experimental evidence indicating that the actin network in the keratocyte lamellipodium is nearly stationary with respect to the substrate[8,13,17]. The rear boundary of the cell is also implicit in our model, and is set by the position of the 'rear corners' of the lamellipodium: the locations at which the density of actin filaments actively pushing against the cell membrane falls to zero. Thus, we do not address the possible contribution of myosin contraction in retracting the cell rear and disassembling the actin network[7,26] (see Supplementary Information).

Our results emphasize that careful quantitative analysis of natural cell-to-cell variation can provide powerful insight into the molecular mechanisms underlying complex cell behaviour. A rapidly moving keratocyte completely rebuilds its cytoskeleton and adhesive structures every few minutes, generating a cell shape that is both dynamically determined and highly robust. This dynamic stability suggests that shape emerges from the numerous molecular interactions as a steady-state solution, without any simple central organizing or bookkeeping mechanism. In this work, we relied on several decades of detailed mechanistic studies on the molecular mechanisms involved to derive a physically realistic model for large-scale shape determination. This model is directly and quantitatively coupled to the molecular-scale dynamics and has surprising predictive power. As individual functional modules within cells are unveiled at the molecular level, understanding their large-scale integration is becoming an important challenge in cell biology. To this end, we propose that the biologically rich cell-to-cell variability present within all normal populations represents a fruitful but currently underused resource of mechanistic information regarding complex processes such as cell motility.

## METHODS SUMMARY

**Cell culture.** Keratocytes were isolated from the scales of the Central American cichlid *H. nicaraguensis* and were cultured as described previously[11]. TMR-derivatized kabiramide C was added to cells in culture medium for 5 min and subsequently washed[20]. DMSO treatment consisted of either application of 2–5 μl DMSO directly onto cells or addition of 10% DMSO to the culture medium.

**Microscopy.** Cells were imaged in a live-cell chamber at room temperature (~23 °C) on a Nikon Diaphot300 microscope using a ×60 lens (numerical aperture, 1.4). To obtain velocity information, for each coverslip, 15–30 randomly chosen cells were imaged twice, 30 s apart. Time-lapse movies of individual cells were acquired at 10-s intervals.

**Shape analysis.** Cell morphology was measured from manually defined cell shapes, as described previously[11,19]. 'Shape modes' were produced by performing principal components analysis on the population of cell shapes after mutual alignment.

**Full Methods** and any associated references are available in the online version of the paper at www.nature.com/nature.

**Received 14 December 2007; accepted 31 March 2008.**

1. Carlier, M. F. & Pantaloni, D. Control of actin assembly dynamics in cell motility. *J. Biol. Chem.* **282,** 23005–23009 (2007).
2. Pollard, T. D., Blanchoin, L. & Mullins, R. D. Molecular mechanisms controlling actin filament dynamics in nonmuscle cells. *Annu. Rev. Biophys. Biomol. Struct.* **29,** 545–576 (2000).
3. Zaidel-Bar, R., Cohen, M., Addadi, L. & Geiger, B. Hierarchical assembly of cell-matrix adhesion complexes. *Biochem. Soc. Trans.* **32,** 416–420 (2004).
4. Bakal, C., Aach, J., Church, G. & Perrimon, N. Quantitative morphological signatures define local signaling networks regulating cell morphology. *Science* **316,** 1753–1756 (2007).
5. Anderson, K. I. & Cross, R. Contact dynamics during keratocyte motility. *Curr. Biol.* **10,** 253–260 (2000).
6. Lee, J. & Jacobson, K. The composition and dynamics of cell–substratum adhesions in locomoting fish keratocytes. *J. Cell Sci.* **110,** 2833–2844 (1997).
7. Svitkina, T. M., Verkhovsky, A. B., McQuade, K. M. & Borisy, G. G. Analysis of the actin–myosin II system in fish epidermal keratocytes: mechanism of cell body translocation. *J. Cell Biol.* **139,** 397–415 (1997).
8. Theriot, J. A. & Mitchison, T. J. Actin microfilament dynamics in locomoting cells. *Nature* **352,** 126–131 (1991).
9. Euteneuer, U. & Schliwa, M. Persistent, directional motility of cells and cytoplasmic fragments in the absence of microtubules. *Nature* **310,** 58–61 (1984).
10. Goodrich, H. B. Cell behavior in tissue cultures. *Biol. Bull.* **46,** 252–262 (1924).
11. Lacayo, C. I. *et al.* Emergence of large-scale cell morphology and movement from local actin filament growth dynamics. *PLoS Biol.* **5,** e233 (2007).
12. Lee, J., Ishihara, A., Theriot, J. A. & Jacobson, K. Principles of locomotion for simple-shaped cells. *Nature* **362,** 167–171 (1993).

13. Jurado, C., Haserick, J. R. & Lee, J. Slipping or gripping? Fluorescent speckle microscopy in fish keratocytes reveals two different mechanisms for generating a retrograde flow of actin. *Mol. Biol. Cell* **16,** 507–518 (2005).
14. Kucik, D. F., Elson, E. L. & Sheetz, M. P. Cell migration does not produce membrane flow. *J. Cell Biol.* **111,** 1617–1622 (1990).
15. Grimm, H. P., Verkhovsky, A. B., Mogilner, A. & Meister, J. J. Analysis of actin dynamics at the leading edge of crawling cells: implications for the shape of keratocyte lamellipodia. *Eur. Biophys. J.* **32,** 563–577 (2003).
16. Prass, M., Jacobson, K., Mogilner, A. & Radmacher, M. Direct measurement of the lamellipodial protrusive force in a migrating cell. *J. Cell Biol.* **174,** 767–772 (2006).
17. Vallotton, P. *et al.* Tracking retrograde flow in keratocytes: news from the front. *Mol. Biol. Cell* **16,** 1223–1231 (2005).
18. Cootes, T. F., Taylor, C. J., Cooper, D. H. & Graham, J. Active shape models — their training and application. *Comput. Vis. Image Underst.* **61,** 38–59 (1995).
19. Pincus, Z. & Theriot, J. A. Comparison of quantitative methods for cell-shape analysis. *J. Microsc.* **227,** 140–156 (2007).
20. Petchprayoon, C. *et al.* Fluorescent kabiramides: new probes to quantify actin *in vitro* and *in vivo*. *Bioconjug. Chem.* **16,** 1382–1389 (2005).
21. Tanaka, J. *et al.* Biomolecular mimicry in the actin cytoskeleton: mechanisms underlying the cytotoxicity of kabiramide C and related macrolides. *Proc. Natl Acad. Sci. USA* **100,** 13851–13856 (2003).
22. Sanger, J. W., Gwinn, J. & Sanger, J. M. Dissolution of cytoplasmic actin bundles and the induction of nuclear actin bundles by dimethyl sulfoxide. *J. Exp. Zool.* **213,** 227–230 (1980).
23. Watanabe, N. & Mitchison, T. J. Single-molecule speckle analysis of actin filament turnover in lamellipodia. *Science* **295,** 1083–1086 (2002).
24. Pollard, T. D. & Borisy, G. G. Cellular motility driven by assembly and disassembly of actin filaments. *Cell* **112,** 453–465 (2003).
25. Wang, Y. L. Exchange of actin subunits at the leading edge of living fibroblasts: possible role of treadmilling. *J. Cell Biol.* **101,** 597–602 (1985).
26. Kozlov, M. M. & Mogilner, A. Model of polarization and bistability of cell fragments. *Biophys. J.* **93,** 3811–3819 (2007).
27. Sheetz, M. P., Sable, J. E. & Dobereiner, H. G. Continuous membrane–cytoskeleton adhesion requires continuous accommodation to lipid and cytoskeleton dynamics. *Annu. Rev. Biophys. Biomol. Struct.* **35,** 417–434 (2006).
28. Schaus, T. E. & Borisy, G. Performance of a population of independent filaments in lamellipodial protrusion. *Biophys. J.* (in the press).
29. Footer, M. J., Kerssemakers, J. W., Theriot, J. A. & Dogterom, M. Direct measurement of force generation by actin filament polymerization using an optical trap. *Proc. Natl Acad. Sci. USA* **104,** 2181–2186 (2007).
30. Kovar, D. R. & Pollard, T. D. Insertional assembly of actin filament barbed ends in association with formins produces piconewton forces. *Proc. Natl Acad. Sci. USA* **101,** 14725–14730 (2004).
31. Parekh, S. H., Chaudhuri, O., Theriot, J. A. & Fletcher, D. A. Loading history determines the velocity of actin-network growth. *Nature Cell Biol.* **7,** 1219–1223 (2005).
32. Mitchison, T. J. & Cramer, L. P. Actin-based cell motility and cell locomotion. *Cell* **84,** 371–379 (1996).
33. Ridley, A. J. *et al.* Cell migration: integrating signals from front to back. *Science* **302,** 1704–1709 (2003).
34. Raucher, D. & Sheetz, M. P. Cell spreading and lamellipodial extension rate is regulated by membrane tension. *J. Cell Biol.* **148,** 127–136 (2000).

**Supplementary Information** is linked to the online version of the paper at www.nature.com/nature.

**Acknowledgements** We thank C. Lacayo, C. Wilson and M. Kozlov for discussion, and P. Yam, C. Lacayo, E. Braun and T. Pollard for comments on the manuscript. K.K. is a Damon Runyon Postdoctoral Fellow supported by the Damon Runyon Cancer Research Foundation, and a Horev Fellow supported by the Taub Foundations. A.M. is supported by the National Science Foundation grant number DMS-0315782 and the National Institutes of Health Cell Migration Consortium grant number NIGMS U54 GM64346. J.A.T. is supported by grants from the National Institutes of Health and the American Heart Association.

**Author Contributions** Z.P., K.K., E.L.B., G.M.A. and J.A.T. designed the experiments. K.K., G.M.A., E.L.B. and Z.P. performed the experiments. Z.P. together with K.K., A.M., G.M.A. and E.L.B. analysed the data. A.M. together with K.K., Z.P., E.L.B., G.M.A. and J.A.T. developed the model. G.M. provided the kabiramide C probe. Z.P., K.K., A.M. and J.A.T. wrote the paper. All authors discussed the results and commented on the manuscript.

**Author Information** Reprints and permissions information is available at www.nature.com/reprints. Correspondence and requests for materials should be addressed to J.A.T. (theriot@stanford.edu).

## METHODS

**Cell culture.** Keratocyte sheets from one-day-old cultures were disaggregated by incubating in 85% PBS and 2.5 mM EGTA, pH 7.4, for 5 min, followed by incubation in normal media for an additional ~1–2 h. TMR-derivatized kabiramide C was added to cells in culture medium for 5 min and subsequently washed[20]. Pharmacological agents including, cytochalasin D (Sigma), latrunculin, jasplakinolide (both from Molecular Probes), blebbistatin (active enantiomer, Toronto Research Chemicals) or calyculin A (Upstate), were applied to cells in culture medium, and the cells were imaged 10–30 min afterwards.

**Microscopy.** Images were collected on a cooled back-thinned CCD camera (Princeton Instruments), with a ×2 optovar attached (1 pixel = 0.11 μm). The population data was acquired by imaging 15–30 randomly chosen cells per coverslip.

**Shape analysis.** Cell morphology was measured from cell shapes represented as polygonal outlines and mutually aligned, as described previously[11,19]. In brief, cell shapes were manually masked using the magnetic-lasso tool in Adobe Photoshop on the phase-contrast image and stored as binary images. Polygonal outlines were extracted from these masks and represented as two-dimensional parametric periodic uniform cubic B-splines, which were sampled at 200 evenly spaced points to generate the final polygons. These were then aligned across the population to ensure that all polygons were oriented similarly; to facilitate this, the centroid of the cell body—a landmark by which the front and rear of the cell can be automatically determined—was extracted from the fluorescent kabiramide C image or by manual marking. Simultaneously, the point ordering of each polygon was adjusted so that corresponding points were in similar spatial locations on the cell across the population. (See algorithms 1 and 2 in Supplementary Information for details.) Cell alignment was then manually verified. The 'shape modes' were produced by applying the principal components analysis to the population of cell shapes, represented as 400-dimensional vectors of packed $(x, y)$ points, and scaled in terms of the standard deviation of the population of shapes along that principle component.

Measured cellular characteristics included: cell area; aspect ratio; lamellipodial radius; speed; front roughness; and actin ratio. Area was measured directly from the polygons with the standard formula. Aspect ratio was measured as the ratio of the width to the length of the cell's bounding box after cells were mutually aligned as above. The roughness of the leading edge of each cell was measured by calculating the average absolute value of the local curvature at each point along the leading edge, corrected for effects due to cell size[11]. The overall curvature of the leading edge was calculated as the radius of the least-squares 'geometric fit' of a circle to the points corresponding to the leading edge (the forward 40% of the cell)[35]. The distribution of kabiramide C staining along the leading edge was calculated by averaging the intensity of background-corrected fluorescence images between the cell edge (as determined by the polygon) and 1 μm inward from there. The centre intensity was defined as the average of this profile in a 5-μm-wide window centred on the cell midline; side intensity was defined as the average in similar windows at the left and right sides of the cell. Cell speed for the live population data was extracted from the displacement of the cell centroid as determined from the manually drawn masks of the two images taken 30 s apart for each cell. Angular cell speed was extracted from the relative rotation angle required for alignment of the two cell shapes. For time-lapse movies of individual cells and DMSO-treated cells taken with a 10-s time interval, the centroid based measurements were noisy so we relied on a correlation-based technique[36]. The translation and rotation of a cell between a pair of consecutive time-lapse images were extracted as in ref. 36, with the modification that the masks used were based on the manually drawn cell masks and the centre of rotation was taken as the centroid of the mask in the first image. All measurements of individual cells (unstained, stained with kabiramide C, and perturbed, as well as a fixed-cell population) and on cells followed with time-lapse microscopy (stained with kabiramide C and perturbed with DMSO) are provided as Supplementary Tables.

To assess the significance of the reported correlations between measurements in a manner reasonably robust to outliers, we used the bootstrap method to approximate the sampling distribution of each correlation coefficient $r$. The data set was resampled with replacement $10^4$ times, and for each resampling the pairwise correlations were recomputed. Positive (or negative) correlations were deemed significant if $r = 0$ fell below the 5th (or above the 95th) percentile of the estimated distribution of $r$. Differences in the mean values of each measure between the perturbed and unperturbed populations were assessed for significance with the same procedure.

35. Gander, W., Golub, G. H. & Strebel, R. Least-squares fitting of circles and ellipses. *BIT* **34**, 558–578 (1994).
36. Wilson, C. A. & Theriot, J. A. A correlation-based approach to calculate rotation and translation of moving cells. *IEEE Trans. Image Process.* **15**, 1939–1951 (2006).

# Mechanism of shape determination in motile cells

## Supplementary Table 1: Model Assumptions

| Assumption | Rationale for assumption | Level of confidence in assumption | How critical is the assumption |
|---|---|---|---|
| There is a constant number of branching events per second per cell. | It produces prediction of the scaling property of the graded actin filament density that many models fail to produce[1]. | Moderate | Moderately critical; other models could predict graded density. |
| The density of pushing filaments at the rear corners of the lamellipodium is zero. | It is likely that this density is small; assuming it zero simplifies the model and produces excellent parameter-less fit. | Moderate | Moderately critical; assuming a small, non-zero density produces reasonable fits as well. |
| Membrane tension is spatially constant. | Known for in vitro membrane physics; see estimates in this paper. | High | Highly critical. |
| Cell shape can be approximated by a slightly bent rectangle. | Shape analysis. | High | Not very critical; it makes the model algebra much easier. |
| Membrane resistance is distributed equally locally among the growing filaments. | Theoretical arguments previously published[2,3]. | High | Highly critical. |
| Protrusion is force-limited; the force–velocity relation is concave down. | Indirectly indicated by our data; previously published measurements[4,5]. | High | Highly critical. |
| Filaments grow on average in a direction locally normal to the boundary. | Previously published work[6]. | Moderate | Moderately critical; other mechanisms would complicate the model. |
| Growing filaments are stalled or buckled at the cell sides. | Speculation | Moderate | Highly critical; this is the central assumption of our force-balance model. |
| Myosin-powered contraction produces a significant centripetal actin network flow only at the very rear of the cell. | Measurements of actin network flow[7]. | High | Not very critical; otherwise, relatively small corrections to the model required. |

# Supplementary discussion

## *1. Mathematical model of cell shape*

### Sub-model of actin filament distribution along the leading edge

Following our previous work[8], we observe that the actin network is organized in a dendritic array with actin filaments oriented at approximately $\pm 35^o$ relative to the direction of protrusion, and model the densities of right- and left-oriented growing barbed ends along the leading edge with functions $b^{\pm}(l,t)$. We assume that Arp2/3-mediated filament branching takes place at the same rate for each leading-edge filament. This per-filament rate is equal to the total number of filaments nucleated over the whole leading edge per second divided by the total number of the uncapped leading-edge filaments. The molecular pathway determining this rate is unknown; a plausible mechanism could be based on rapidly diffusive molecules, the total number of which is conserved, controlling the total number of branching events per cell. Assuming that the branching takes place only along the leading edge, each filament has equal probability to become a "mother" filament. Then, as the total number of growing filament ends increases, the branching rate per filament decreases inversely. A filament at $+35^o$ branches off filaments oriented at $-35^o$, and vice versa. As filaments are skewed with respect to the direction of protrusion, their barbed ends slide laterally along the leading edge as they grow. Finally, the filaments get capped and lag behind the leading edge. These assumptions lead to the following equations for the densities of growing barbed ends along the leading edge:

$$\underbrace{\frac{\partial \mathrm{b}^{\pm}}{\partial \mathrm{t}}}_{\substack{\text{rate of}\\ \text{density}\\ \text{change}}} = \underbrace{\mp V \frac{\partial \mathrm{b}^{\pm}}{\partial l}}_{\substack{\text{lateral}\\ \text{flow}}} + \underbrace{\frac{\beta \mathrm{b}^{\mp}}{\mathrm{B}}}_{\text{branching}} - \underbrace{\gamma \mathrm{b}^{\pm}}_{\text{capping}}, \underbrace{\mathrm{B} = \int_{-L/2}^{L/2} \left[\mathrm{b}^{+}(l,t) + \mathrm{b}^{-}(l,t)\right] dl}_{\text{total number of filaments at the leading edge}} \qquad (1)$$

Here $V$ is the lateral flow rate (which is close to cell speed), $l$ is the arc length along the leading edge, $\gamma$ represents the constant rate of capping and $\beta$ is the total number of nascent filaments branching out per cell per second. The actual lateral flow rate is graded along the leading edge (rather than constant as assumed here) due to the curvature of the leading edge, but this does not affect the results, as the respective term is but a small perturbation[8].

We choose the boundary conditions at the rear corners of the leading edge, $l = \pm L/2$ (where $L$ is the total length of the leading edge) as follows:

$$\mathrm{b}^{+}(-L/2, \mathrm{t}) = 0, \mathrm{b}^{-}(L/2, \mathrm{t}) = 0 \qquad (2)$$

The biological meaning of these conditions is that at the rear sides of the leading edge, where large adhesions are located[9], the "age" of any right (left)-oriented filaments at $-L/2$ ($+L/2$) is zero, since they immediately glide to the right (left) away from the side. These boundary conditions are the simplest possible ones, but others are also possible (discussed previously[8]). Note that the solutions of (1-2) derived below have the following feature: $\mathrm{b}^{+}(\pm L/2, \mathrm{t}) + \mathrm{b}^{-}(\pm L/2, \mathrm{t}) \approx 0$, so the total barbed end density at the rear corners

of the leading edge is close to zero according to this model. We chose these boundary conditions because they fit the data well. These conditions would occur naturally if branching ceased at the large adhesions located at the rear corners of the leading edge, where vigorous actin network flow and remodeling take place. Regardless of the exact mechanism, we assume that there are specific local conditions responsible for maintaining a constant, very low density of uncapped barbed ends at the sides. All the modeling results remain valid if the boundary conditions at the sides are changed from zero to a low but non-zero density (at least 4-5 times lower than that at the center).

To non-dimensionalize equations (1-2), we choose the cell's leading edge length, $L$, as the length scale; the characteristic time of capping, $\bar{t} = 1/\gamma$, as the time scale; and the total number of nascent filaments branched out per unit length of the leading edge over the characteristic time scale, $\hat{\mathrm{b}} = \beta \bar{t} / L$, as the filament density scale. This allows us to rescale the equations introducing the non-dimensionalized time, distance and densities: $\mathrm{t} = \bar{t}\, t = \frac{1}{\gamma} t$, $l = Ls$, $\mathrm{b}^{\pm} = \hat{\mathrm{b}} b^{\pm} = \frac{\beta}{L\gamma} b^{\pm}$, respectively. Substitution of these non-dimensional variables into equations (1-2) leads to the non-dimensional system:

$$\frac{\partial b^{\pm}}{\partial t} = \mp\lambda \frac{\partial b^{\pm}}{\partial s} + \frac{b^{\mp}}{B} - b^{\pm}, B = \int_{-1/2}^{1/2} \left[ b^{+} + b^{-} \right] ds, b^{+}\left(-1/2, t\right) = 0, b^{-}\left(1/2, t\right) = 0. \quad (3)$$

Here $\lambda = V / \left(\gamma L\right)$. The capping rate, $\gamma$, is of the order of 1/sec[10], the lateral flow rate $V \sim 0.1 \mu m / \sec$, and the leading edge length $L \sim 30 \mu m$. Thus, in the biologically relevant regime, barbed ends are capped within seconds, long before they move laterally across the leading edge: $\lambda \sim 0.01 << 1$. We are interested in the steady state actin distribution, so equations (3) becomes,

$$\mp\lambda \frac{db^{\pm}}{ds} + \frac{b^{\mp}}{B} - b^{\pm} = 0. \quad (4)$$

Equations (4) can be solved with the standard substitution, $b^{+} = c_{+} \cdot \exp\left(\kappa s\right), b^{-} = c_{-} \cdot \exp\left(\kappa s\right)$, which turns the differential equations (4) into an algebraic system: $\begin{bmatrix} \left(1+\lambda\kappa\right) & -\frac{1}{B} \\ -\frac{1}{B} & \left(1-\lambda\kappa\right) \end{bmatrix} \times \begin{bmatrix} c_{+} \\ c_{-} \end{bmatrix} = \begin{bmatrix} 0 \\ 0 \end{bmatrix}$. This system has a non-trivial solution if $\det \begin{bmatrix} \left(1+\lambda\kappa\right) & -\frac{1}{B} \\ -\frac{1}{B} & \left(1-\lambda\kappa\right) \end{bmatrix} = 0$, leading to the equation $\frac{1}{B^2} = 1 - \lambda^2\kappa^2$ (below, we demonstrate that $\left|\kappa\right| \sim 1$, and so $B \approx 1$ and $b^{+} \approx b^{-}$, so the local densities of left- and right-oriented filaments are almost equal). This equation with the boundary condition (3) allows two solutions, both with $\kappa$ an imaginary number: $\kappa = \pm i\kappa_0, \kappa_0 = \frac{1}{\lambda}\sqrt{\frac{1}{B^2} - 1}$. Then,

$\begin{bmatrix} b^+ \\ b^- \end{bmatrix} \approx C_1 \begin{bmatrix} 1 \\ 1 \end{bmatrix} \exp(\kappa_0 s) + C_2 \begin{bmatrix} 1 \\ 1 \end{bmatrix} \exp(-\kappa_0 s)$. Due to the symmetry of the problem, $C_1 = C_2 = C$, and $b^+ \approx b^- \approx C\cos(\kappa_0 s)$ (the $\sin(\kappa_0 s)$ term disappears due to the symmetry). A system of three equations then determines three unknowns, $B, C, \kappa_0$:

$$B \approx \frac{4C}{\kappa_0}\sin(\kappa_0/2), B^2 = \frac{1}{1+\lambda^2\kappa_0{}^2}, C\cos(\kappa_0/2) = 0 \quad (5)$$

From (5), we find $\kappa_0 \approx \pi, B \approx 1, C \approx \pi/4$. The approximate analytical solution for the stationary non-dimensional actin filament density along the leading edge, $b^+ + b^- \approx (\pi/2)\times\cos(\pi s)$, is in excellent agreement with the numerical solution[8], as well as with the data (Fig. 3b; see also Lacayo *et al.*[8]). Specifically, the actin filament density distribution exhibits the predicted scaling – the distribution is a function of the ratio of *l/L* – so when the distance is scaled by cell length, and the density by its maximal value, the distributions in all cells are similar.

The predicted dimensional actin filament distribution has the form:

$$D(l) = \mathrm{b}^+(l) + \mathrm{b}^-(l) = \frac{\pi}{2}\frac{\beta}{L\gamma}\cos\left(\frac{\pi l}{L}\right) \quad (6)$$

This distribution has a concave down profile with a maximum $\sim\beta/\gamma L$ at the center of the edge and a minimum ~ 0 at the rear side corners. For the following, we approximate this distribution with an inverted parabolic function (Fig. 3c):

$$D(l) = \frac{\beta}{L\gamma}\left(1 - \left(\frac{l}{L/2}\right)^2\right) \quad (7)$$

This approximation to the trigonometric function is very close and makes all subsequent algebra much simpler. We tested the results from all formulae derived from this approximation against those from the trigonometric equations and found that the results are not affected by this approximation.

With the model's boundary conditions, more nascent filaments branch out closer to the center of the cell. This, in turn, increases the net branching rate at the center, because more nascent filaments branch off the higher number of the existing filaments at the center. The existing growing barbed ends start to effectively compete for resources (because the total number of branching events per second is conserved), and if the actin filament density at the cell sides is kept low, the center 'wins'. This positive feedback is the reason for the characteristic inverted parabolic profile of the actin filament distribution.

It is worth mentioning that our measurements show inverted parabolic actin filament distributions along the central part of the leading edge, as predicted. However, the filamentous actin density at the sides does not decrease significantly from the front corners to the rear corners, so we cannot directly test the validity of the boundary conditions (the parameter-free fit of the prediction to the data (see below) is an indirect test). Our explanation of why the measured actin filament density at the sides does not

decrease significantly hinges on the fact that with actin labeling experiments we cannot distinguish between growing, pushing filaments (the density of which is expected to decrease), and capped/stalled/buckled filaments. According to the model, actin filaments are either stalled or buckled at the front side corners of the lamellipodium. These stalled/buckled filaments contribute to the measured filamentous actin density along the lamellipodial sides, but do not contribute to protrusion. As the cell moves forward, more stalled/buckled filaments accumulate towards the rear of the lamellipodial sides, so the fraction of the filamentous actin density that is due to those filaments has to grow from front to rear along the sides. Thus, the fact that the measured filament density along the sides is more or less constant likely indicates that the density of growing, pushing filaments indeed decreases from front to rear at the sides.

Finally, note that according to the model, the actin filament density along the leading edge is proportional to the density of the uncapped growing barbed ends there. The density of uncapped growing barbed ends at the leading edge is approximately determined by the following balance: $db/dt = (\beta/B) - \gamma b$. On the other hand, the density of capped barbed ends increases due to capping and decreases due to the fact that capped ends cease to grow and thus lag behind the cell front (which continues to protrude with rate $V$). Thus, within a narrow zone of width $u$ at the leading edge, the density, $c$, of the capped barbed ends is determined by the following balance: $dc/dt = \gamma b - (V/u)c$, where the rate of the capped ends leaving the edge is equal to the width of the zone divided by the protrusion rate. At steady state, $b = (\beta/\gamma B)$, and $c = (\gamma u/V)b$. The total number of the leading edge filaments is thus, $(c+b) = \left[1+\frac{\gamma u}{V}\right] b$. The natural scale for the parameter $u$ is the average actin filament length, which is of the order of $(V/\gamma)$. Thus, the factor $\left[1+\frac{\gamma u}{V}\right]$ is a dimensionless parameter of order unity, which is independent of any cell-dependent variables, so the total density of actin filaments at the leading edge, both capped and uncapped, is proportional to the capped filaments' density there. The actin filament number density, in turn, is proportional to the total density of filamentous actin at the leading edge.

**Cell geometry**

As illustrated by our shape analysis (Fig. 1b), keratocyte shapes can be largely described by two parameters – shape modes 1 and 2, mostly corresponding to cell area and aspect ratio, respectively. Thus, keratocyte shapes can be approximated reasonably well by a simple geometric figure, such as a rectangle (inset, Fig. 3d).

Let us assume therefore that the lamellipodium is a rectangle characterized by its area ($A$) and aspect ratio ($S$), or alternatively by its length ($x$) and width ($y$), so that $xy = A, x/y = S$. Note, that the total leading edge length is, $L = x + 2y$. The following are obvious geometric relations:

$$x = \sqrt{AS}, y = \sqrt{A/S}, L = \sqrt{AS} + 2\sqrt{A/S} \quad (8)$$

For the observed range of aspect ratios, $1 < S < 4$, the total leading edge length varies only ~ 10% as the aspect ratio varies 4-fold, and the approximate expression for this length is $L \approx 3\sqrt{A}$, which is supported by the data.

The validity of the rectangular approximation is supported by the observation that across the population of cells, the measured perimeter ( $P_m$ ) is nearly equal to the perimeter calculated from the rectangle approximation using each cell's measured area and aspect ratio, $P_c = 2(x+y) = 2\left(\sqrt{AS} + \sqrt{A/S}\right)$ (Fig. S7). It is worth noting that keratocyte shapes could also be approximated by other relatively simple geometric figures quantified by two parameters, such as a half-ellipse, rather than a rectangle. In those cases, a model similar to the one presented here could be built and similar predictions would be generated, though the algebra would become much more involved. Note however, that in most cases, the shapes qualitatively appear more rectangular than half-elliptical (Fig. 1a), so such approximation apart from being less tractable would also lead to larger errors.

Let us also note that approximating the actual cell shape by a rectangular one introduces small errors that are hard to control. For example, both the front and the sides of cells are convex, and we, in fact, estimate the leading edge curvature below. Rough geometric estimates (not shown) indicate that this could lead to systematic under-estimation of the leading edge length by ~ 10-20%. Also, there are small ambiguities in the locations of the front and rear corners in real cells, and therefore in the appropriate boundary conditions. The accumulated errors jeopardize neither the orders of magnitude of the theoretical estimates, nor the predicted correlations between variables; however, together with experimental errors and stochastic effects in cell behavior, this limits our ability to make exact fits and calculations at this point.

**Force balance determines cell shape**

A growing actin network can be characterized by the so-called force–velocity relation[11]. When no force resists filament growth, protrusion occurs at the free polymerization rate $V_0$. The free polymerization rate is equal to $V_0 = k_{on}\delta G - k_{off}\delta$, where $k_{on} \approx 10/(\mu M \cdot \sec)$ and $k_{off} \approx 1/(\sec)$ are, respectively, the monomer assembly and dissociation rates at the barbed ends of actin filaments[10], $\delta \approx 3nm$ is the length increment of a filament upon an assembly event, and *G* is the actin monomer concentration at the leading edge. Note that $k_{off}\delta \sim 1nm/s << V_0$, so we can approximate the free polymerization rate as, $V_0 \approx k_{on}\delta G$. As the load force, *f*, applied to a filament's barbed end increases, the protrusion rate, $V$, decreases until at the stall force, $f_{stall}$, it ceases. Thus, $V(f=0) = V_0, V(f = f_{stall}) = 0$. In this force–velocity relation the force is per filament. The stall force per filament, $f_{stall} \sim 2-3pN$, has been measured, albeit

indirectly[12,13]. In fact, longer filaments can buckle[14] rather than stall; the resistance could bend a filament so that it starts to grow in parallel with the boundary, which is equivalent to stalling protrusion. There are experimental indications that this buckling mechanism is plausible in motile cells[15]; estimates show that with the observed lengths and elastic properties of actin filaments, the buckling force would be of the same order of magnitude as the stall force[16]. Whether filaments in motile keratocytes are buckled or stalled at the sides is an unresolved question that will also depend on the local mesh organization.

In the lamellipodium, the membrane resistance force is distributed among neighboring filaments almost equally[2], so the force per filament can be approximated by $f = T / D$. Here $T$ is the membrane tension (force per unit length of the cell boundary), which, as described below, is spatially constant (but can, in principle, fluctuate in time). As $D$, the number of pushing barbed ends per unit length of the boundary, is graded in space, the force per filament also varies along the leading edge with a minimum at the center and increasing toward the sides. In subsequent derivations, we use the following notations: the actin filament density at the center of the leading edge is denoted $D_c$, and from (7), $D_c = \beta / (L\gamma)$. At the sides of the front edge defined by $l = \pm x/2$, the density is $D_s = \frac{\beta}{L\gamma}\left(1-\left(\frac{x}{L}\right)^2\right)$. Finally, we denote the ratio $D_c/D_s$ *as* $D_{cs}$.

It is very convenient to introduce the lumped model parameter:

$$z = \frac{T\gamma}{f_{stall}\beta} \tag{9}$$

which is the ratio of membrane tension to the total force needed to stall the network of growing actin filaments at the central lamellipodium. Recall that $D_c = \beta / (\gamma L)$, so

$$\frac{T}{f_{stall}D_c} = \frac{T\gamma L}{f_{stall}\beta} = zL\,. \tag{10}$$

We assume that the sides of the leading edge are defined by where filaments are mechanically stalled by the membrane tension: $V_s = 0, T / (f_{stall}D_s) = 1$. Then, $T = f_{stall}\frac{\beta}{L\gamma}\left(1-\left(\frac{x}{L}\right)^2\right)$, or,

$$z = \frac{1}{L}\left(1-\left(\frac{x}{L}\right)^2\right). \tag{11}$$

From (8), $\frac{x}{L} = \frac{S}{S+2}$, $1-\left(\frac{x}{L}\right)^2 = \frac{4(S+1)}{(S+2)^2}$, and $\frac{1}{L} = \frac{\sqrt{S}}{\sqrt{A(S+2)}}$ so,

$$z = \frac{4\sqrt{S}\,(S+1)}{\sqrt{A}\,(S+2)^3}, \tag{12}$$

and (see also Fig. 3d),

$$D_{cs} = \frac{D_c}{D_s} = \left[1 - \left(\frac{x}{L}\right)^2\right]^{-1} = \frac{(S+2)^2}{4(S+1)}, zL = \frac{1}{D_{cs}} = \frac{4(S+1)}{(S+2)^2}. \quad (13)$$

**Force–velocity relation determines leading edge radius**

The shape of the lamellipodium in real cells is obviously rounded (Fig. 1a). Thus to further characterize lamellipodial shape, in addition to length and width, we introduce the approximate leading edge radius, *R*. The rounded shape of the leading edge of motile keratocytes is maintained through a graded distribution of protrusion along the edge[6]. As explained in the main text, we hypothesize that membrane tension is the crucial limiting factor for filament elongation and protrusion, and explain the curvature of the leading edge as follows. At the maximal actin filament density in the middle of the leading edge, the load imposed by membrane tension is carried by many filaments and thus the force per filament is small, so filament growth rate is high. Toward the sides, the filament density decreases and the load per filament gradually increases, so the growth rate decreases. This smoothly decreasing growth rate toward the sides of the lamellipodium then leads to a curved leading edge. While the exact form of the force–velocity relation was not required above in determining the approximate cell shape (i.e. the cell aspect ratio in the rectangular shape approximation), it is required for the calculation of the effective curvature of the leading edge described below as well as for determining the relationship between cell speed and cell morphology discussed in the next section.

The force–velocity relation for individual actin filaments has not been measured directly (theory suggest that it is concave up, or more complex: concave down at small forces and concave up at greater loads[2,11]). Moreover, the single filament force–velocity relation does not directly determine the relation for a network of actin filaments; while the stall force for a network of filaments is approximately equal to the stall force per filament times the number of filaments, the network force–velocity relation elsewhere is not simply obtained from the individual filament relation assuming the force is divided by the filament number. One possible reason for this is the existence of a mechanochemical feedback between filament number and force. In the most extreme form of this feedback[17], the filament number is proportional to force, so that velocity is simply independent of force until the whole network crushes at the stall force. This extreme case would lead to a step-function-like force–velocity relation (and in our case, a rectangular shaped cell as the protrusion rate along the front of the leading edge would be uniform). Other reasons for a more complicated network force–velocity relation include properties of force-sensitive adhesions and elastic recoil of the actin network (discussed elsewhere[5]).

In a very general form, the force–velocity relation can be expressed by the formula:

$$V = V_0\left(1 - \left(\frac{f}{f_{stall}}\right)^w\right). \quad (14)$$

(There are many other elementary functions that could be used to express this relation, e.g. $\left(1+\exp\left[w\left(f-f_{stall}\right)\right]\right)^{-1}$; the results do not depend on the particular choice of functions, but the calculations are simplest when power functions of the force are used.) By varying the parameter $w$, all ever-observed force–velocity relations can be approximated, except for a few cases where non-monotonic[18], or crossover[19] relations were predicted or observed. In the latter cases, the mechanism involved is too complex or not well understood, so at present such cases are ignored.

The parameter $w$ determines how robust protrusion is. If $w = 1$, the protrusion rate decreases linearly with increasing resistive force; at half the stall force, the protrusion rate goes at half the free polymerization rate. If $w < 1$, the force–velocity relation is concave up, so the protrusion rate decreases rapidly with small increases in the resistive force; at half the stall force, the protrusion rate is less than half the free polymerization rate. Such a concave up force–velocity relation was measured, for example, for *in vitro* actin networks assembled from purified proteins[20]. These results, however, do not agree with a more directly relevant measurement performed on the lamellipodial network in fish keratocytes which showed a concave down force–velocity relation[5] or with measurements on *in vitro* actin networks assembled in cytoplasmic extracts[21] which are discussed below. Finally, if $w > 1$, the force–velocity relation is concave down, so the protrusion rate decreases slowly with small increasing resistive force; at half the stall force, the protrusion rate is greater than half the free polymerization rate. In this case protrusion is robust: the protrusion rate is nearly constant at loads weak relative to the stall force, while at greater loads the speed decreases drastically. Mathematically, as $w$ increases, the force–velocity relation becomes closer to a step function. We show the shapes of the force–velocity relations given by (14) for $w$ =1,2,4,8 (Fig. S6b).

Direct measurements in motile keratocytes[5] and in *in vitro* actin networks[21] both resulted in a concave down force–velocity relation that we approximated mathematically, based on the published data, by a relation of the form (14) with $w \approx 4$ (fits not shown). However, the value of the parameter $w$ is by no means established for the force–velocity relation characterizing a lamellipodium that is protruding steadily. It is notoriously difficult to measure the force–velocity relation and interpret the results of those measurements. Moreover, both cited experimental studies did not measure the force–velocity curve directly, but rather derived it from dynamic data: the measurements were performed in a transient regime in which growing actin networks were slowed down rapidly, over seconds, by increasing the force imposed by an AFM cantilever. There is no guarantee that actin networks in such experiments have enough time to adjust to changing conditions (the characteristic time of network re-modeling is in the second to tens of seconds range[11]), and indeed one of the studies found hysteresis behavior[21]. It is therefore plausible that in a steadily protruding network, the actin architecture adapts to achieve a more robust force–velocity relation that is less sensitive to the resistive force, so the actual force–velocity relation would be characterized by a more step-like function with $w > 4$.

Assuming that filaments grow in a direction locally normal to the boundary, and taking into account the persistence of keratocyte shape through time [6,22], we can relate the

angle between the normal to the cell edge and the direction of crawling with the local filament growth rate (Fig. S6a):

$$\cos\theta(l) = V(l)/V(0) \tag{15}$$

where $\theta(l)$ is the orientation of the normal to the leading edge at position $l$, and $V(l)$ is the normal protrusion rate there; note that $V(0) = V_{cell}$. As the protrusion rate decreases toward the sides, the angle $\theta$ increases leading to the curved leading edge. From trigonometry, for small $l$ and $\theta$, $\cos\theta \approx 1-\theta^2/2$, and $l = R\sin\theta \approx R\theta$, where $R$ is the approximate lamellipodial radius in the middle of the leading edge. So, $R \approx l/\theta$. Taking the force–velocity relation in (14) we have,

$$V(l) = V_0\left(1-\left(\frac{T}{f_{stall}D(l)}\right)^w\right). \tag{16}$$

Using formulae (7, 16) and simple calculus, we find the graded lateral change of the locally normal protrusion rate: $V(l) \approx V_{cell} - \frac{dV}{dD}\frac{D_c}{(L/2)^2}l^2$. Substituting this expression into (15) and using the approximation $\cos\theta \approx 1-\theta^2/2$, we obtain the formula, $1-\theta^2/2 \approx 1-\frac{dV}{dD}\frac{D_c/V_{cell}}{(L/2)^2}l^2$, from which we can express the angle $\theta$ in terms of the coordinate $l$ as $\theta \approx 2\sqrt{\frac{2dV/dD}{V_{cell}/D_c}}\frac{l}{L}$. Thus, $R \approx \frac{l}{\theta} \approx \frac{L}{2}\sqrt{\frac{V_{cell}/D_c}{2dV/dD}}$. Using (10,16), we have: $\frac{V_{cell}}{D_c} = \frac{V_0}{(1/zL)}\frac{d(1/zL)}{dD}\left(1-(zL)^w\right)$ and $\frac{dV}{dD} = wV_0(zL)^{w+1}\frac{d(1/zL)}{dD}$, so $\frac{V_{cell}/D_c}{dV/dD} = \frac{(zL)^{-w}-1}{w}$, finally giving,

$$R \approx L\frac{\sqrt{(zL)^{-w}-1}}{2\sqrt{2w}}. \tag{17}$$

Using equations (8,13), $R$ can now be expressed as a function of cell area and aspect ratio:

$$R \approx \frac{\sqrt{AS}+2\sqrt{A/S}}{2\sqrt{2w}}\sqrt{\left(\frac{4(S+1)}{(S+2)^2}\right)^{-w}-1}. \tag{18}$$

We used (18) to calculate the expected leading edge radius of cells from the measurements of $A$ and $S$ using different force–velocity relations characterized by $w$ = 1,2,4,8, and plotted the predicted versus the measured radii in Fig. S6c. For all these values of the parameter $w$, the theory gives the right order of magnitude for the radius, and correctly predicts its correlations with the area and aspect ratio of the cell. Quantitatively, $w$ = 8 gives a very good fit between experiment and theory.

Note also that this model explains a curious observation: high-aspect-ratio cells have relatively broad (high radius) lamellipodia, which implies uniform protrusion

velocities across the leading edge, yet these cells also have high actin filament density at the cell midline and steep actin density gradients toward the sides. Conversely, low-aspect-ratio cells have round lamellipodia, which imply steeply graded velocity differences, but have relatively flat, uniformly low filamentous actin density profiles. This apparent paradox can be resolved by noting that at high actin densities (low force per filament) the force–velocity relation is saturated, so steep actin-density fall-off does not translate to great changes in velocity along the leading edge; the opposite is true at low actin densities, allowing for relatively flat density profiles to yield highly graded velocities.

**Force–velocity relation determines cell speed**

Cell speed is approximately equal to the protrusion rate at the center of the leading edge since the retrograde actin network flow at the center of the leading edge is very low[7,22-25]. In order to calculate cell speed, again knowledge of the specific dependence of the protrusion rate on the membrane tension-generated resistive load is needed. Taking, as above, the force–velocity relation in (14) and again assuming that the cell speed, $V_{cell}$, is equal to the maximum protrusion rate (found at the middle of the lamellipodium, $l$=0), we obtain,

$$V_{cell} = V_0\left(1-\left(\frac{T}{f_{stall}D_c}\right)^w\right) = V_0\left(1-(zL)^w\right) = V_0\left(1-\left(\frac{4(S+1)}{(S+2)^2}\right)^w\right) \qquad (19)$$

In Fig. S6d, we compare the fits obtained using equation (19) for cell speed as a function of aspect ratio to the data for $w$ = 1,2,4,8. It is clear that $w$ = 1, though qualitatively predicting the correct trend, is quantitatively poor; $w$ = 4 is better, and again $w$ = 8 gives a very good fit. Thus, two experimentally independent observations regarding (a) the relation between cell speed and aspect ratio, and (b) the geometrical relation between the lamellipodial radius and cell area and aspect ratio (previous section), are both well fit by our model when we take $V = V_0\left(1-\left(\frac{f}{f_{stall}}\right)^8\right)$ as the force–velocity relation. Explicitly for cell speed this implies:

$$V_{cell} = Gk_{on}\delta\left(1-(zL)^8\right), \qquad (20)$$

where we have neglected the contribution of the monomer off-rate.

**Membrane physics relevant to the cell shape model**

Experimental and theoretical estimates of physical parameters characterizing the plasma membrane of the cell can be gleaned from the literature[26-27]. Most of the measurements reported were made for pure lipid bilayers; however, the corresponding parameters in biological membranes, when measured, are typically only a few fold different than those in pure lipid bilayers[28], which will not change the order-of-magnitude estimates presented here.

First, we argue that the membrane tension is *spatially* constant; it is the same at the front, side and rear of the cell. This assumption is crucial for our model. The membrane tension can, in principle, change in time, but synchronously at all locations around the cell. The theoretical argument is very straightforward: if there is a difference $\sigma$ in membrane tension between the rear and front in the cell, then the rate of membrane flow would be $v \sim \frac{\sigma x^2}{\eta y}$, where $y$ is the lamellipodial length, $x$ is the lamellipodial width, and $\eta$ is the membrane viscosity. Characteristic viscosity is $\eta \sim 0.01 pN \cdot s / \mu m$ [29,30]; characteristic tension amplitude is $\sigma \sim 100\, pN / \mu m$ [4]; other characteristic values are $y \sim 10\mu m$, $x \sim 30\mu m$. So, the membrane would flow with an enormous rate of $v \sim 10^6 \mu m / s$. Thus, even negligibly small differences in membrane tension $\sim 1 pN / \mu m$ would be diminished to zero by lipid flow in just $\sim 10\mu m / \left(10^4 \mu m / s\right) \sim 0.001 s$. Hence on the scale of seconds and minutes relevant to cell motility, the membrane tension is constant in space. Note that experimentally it is established that there is no lasting membrane flow in keratocytes[31].

Second, simple estimates demonstrate that membrane tension is not due to membrane elasticity, but arises primarily from the resistance of the membrane to actin pushing forces at the front and sides of the cell. At the rear of the cell, this tension is maintained by the actin network's resistance. Let us introduce the effective line tension at the membrane edge, $\Gamma$. The physical meaning of this line tension is the thermodynamic work required to elongate the edge by a unit length. There is a 'horizontal' edge curvature contribution to the line tension; the corresponding free energy per unit area of membrane is equal to $\frac{\kappa}{R^2}$, where $\kappa \sim 20 k_B T$ is the membrane bending modulus[26,32], and *R* is the effective vertical radius of lamellipodial curvature; plus energy of tension $e$ concentrated at the edge. To find $\Gamma$, let us add length $\delta$ to the edge. If *h* is the lamellipodial height, we add a membrane area $a = h\delta$. The effective radius of "vertical" curvature of the edge is simply ~*h*. So, the added energy is $E \sim \left(\frac{\kappa}{R^2} + e\right) \times h\delta \sim \left(\frac{\kappa}{h^2} + e\right) \times h\delta \sim \left(\frac{\kappa}{h} + eh\right) \times \delta$. The effective line tension is $\Gamma = E / \delta \sim \left(\frac{\kappa}{h} + eh\right)$. In this expression, $h \sim 0.1\mu m$ and $\kappa \sim 20 k_B T$. If $e \sim 100\, pN / \mu m$ (see below), then $eh \sim 10\, pN$, while $\frac{\kappa}{h} \sim 1 pN$, so the bending part of the energy can be neglected, and $\Gamma \sim eh$. Now, the actin filament pressure pushing the membrane at the leading edge generated by filaments, *T*, is balanced by the membrane tension, $e$. According to Laplace's Law, if a pressure $(T - e)$ is restrained by a curved membrane boundary under tension, then $\frac{\Gamma}{R} = T - e$, or $e\left(1 + \frac{h}{R}\right) \approx T$. Because $\frac{h}{R} \sim 0.01$, $e \approx T$, so the membrane tension is simply equal to the pressure from the growing actin filaments at the edge.

The magnitude of this pressure can be estimated theoretically; the force per filament is in the pN range[16], and there are ~100 filaments per micron at the leading edge[33], so $T \sim 100\, pN / \mu m$. Tension of similar magnitude was estimated from experiments in which a membrane tether was pulled from the surface of a motile fibroblast[4]. Note, that if this value is substituted into the definition of the lumped parameter *z* in (10), then agreement with the data is achieved if there are a few thousands of pushing filaments per cell, which agrees with previous experimental estimates[33].

This tension is too weak to stretch the membrane significantly: to change membrane area by a few percent, a tension of $\sim 10^5\, pN / \mu m$ is needed[28]. Note also, that the membrane tension is not only constant across the membrane of an individual cell; measurements in a population of fibroblasts suggest that there is little variation in tension across a population of cells[4]. There is also independent evidence that protrusion rate in fibroblasts is limited by membrane tension[4].

The simplest interpretation of our observation that cell area fluctuates only ~1% on the scale of seconds to an hour is that the membrane is pulled taut around the lamellipodium and cell body, and there is very slow exchange of membrane between the exterior cell membrane and its intracellular stores. Indeed, in motile fibroblasts, the endo/exocytosis rate is $\sim 1 \mu m^2 / s$ [28], so about an hour would be needed to replace the plasma membrane; thus it is possible that on the seconds-to-minutes time scale a motile keratocyte keeps cell area constant mechanically. Furthermore, it is known that keratocyte fragments, whose movement is essentially indistinguishable from whole keratocytes, have minimal intracellular membrane stores[34]. Note that we actually measure the projected cell area, rather than the actual cell area. However, since the projected area changes little and the cell is at steady state, all respective areas and volumes, actual and projected, are steady.

The mechanism by which animal cells control their total plasma membrane area is still not well understood[28], and it is possible that cell area is dynamically maintained constant[35]. It is worth keeping in mind that a reservoir of plasma membrane sometimes serves to buffer against fluctuations in the plasma membrane tension for the whole cell, so the membrane tension itself may be maintained constant as well[36], justifying its use as a model parameter. Finally, note that in some cells, a major component of the membrane tension is the energy of transient attachments between the membrane and the actin cytoskeleton[28]. This energy has to be included into the formulae for the energy *E* used above to calculate the membrane tension. Our model corresponds to the assumption that such attachments in motile keratocytes do not contribute significantly; future research will have to test this assumption.

## 2. Model relation to measurements and correlations not addressed explicitly in the main text

### Scaling of model parameters

The lumped parameter *z* is defined in (10) as $z = \frac{T\gamma}{f_{stall}\beta}$. Understanding how these cellular parameters, and *z* overall, scale with large-scale morphological properties like cell area, is of distinct biological interest, as this may provide insight into the biochemical and biophysical mechanisms that determine the value of these parameters. Our model provides a prediction regarding the scaling of *z* with cell geometry: $z(A,S) = \frac{4\sqrt{S}\left(S+1\right)}{\sqrt{A}\left(S+2\right)^3}$, as well as a prediction in terms of the geometrical parameters and the actin distribution ratio: $z(L, D_{cs}) = \frac{1}{L \cdot D_{cs}}$. The predicted dependence of *z* on cell geometry is illustrated in Fig. S5a and b, in which $z(A,S)$ is evaluated at all of the (*A, S*) positions in our dataset and plotted against either *A* or *S.* This demonstrates the general predicted scaling of *z* with these parameters over physiologically-relevant ranges, and also shows that *z* is relatively constant in individual cells through time. The concordance of these two different predictions of the model ($z(A,S)$ and $z(L, D_{cs})$) is shown in Fig. S5c. Note that this concordance is driven entirely by the relation between $D_{cs}$ and *S* shown in Fig. 3: here, we examine the correlation between two different estimates of a cellular parameter, *z*, based on different observables, while Fig. 3 shows the relation between two different observables based on their hypothesized molecular underpinnings.

At present, we cannot simultaneously measure *T*, $\gamma$, $f_{stall}$, and $\beta$ (and hence *z*), so we cannot directly verify the predicted relations. However, we can clarify the model's prediction for specific scaling relations, which are in principle measurable. We expect that $\gamma$ and $f_{stall}$ will not depend on cell size, whereas $\beta$ and $T$ may well vary with cell area. What, then, is the model's prediction of how $T/\beta$ ought to scale with cell area? The expression $z = \frac{4\sqrt{S}\left(S+1\right)}{\sqrt{A}\left(S+2\right)^3}$ obviously implies that $z$, and thus $T/\beta$, vary with cell area. If cell aspect ratio and area were uncorrelated across the population, then we would expect $z \propto A^{-1/2}$; on the other hand, if aspect ratio correlated with area, then *z* would scale differently as a function of area. Detailed analysis of the population data set reveals that cell area and aspect ratio are not independent. Cells with larger area tend to be more canoe-like, illustrated by the fact that the principal axis of shape variation (shape mode 1; Fig. 1b) describes a continuum of shape phenotypes in which area and aspect ratio are coupled. This is further demonstrated by the statistically significant correlation that we observe between cell area and aspect ratio (Fig. 2b; Fig. S2). However, is this dependence enough to substantially modify the predicted scaling of $z \propto A^{-1/2}$? We examined our live

cell data set to find the best-fit exponent $\upsilon$ for the relation $z(A,S) = \tilde{z}A^{\upsilon}$, where $\tilde{z}$ is a constant. The best-fit exponent was $\upsilon = -0.54$ (95% bootstrap confidence interval for $\upsilon$ is [-0.55, -0.53]; Fig. S5d), indicating that the dependence of *S* on *A* influences the scaling of *z* with *A* to a detectable but nevertheless minor degree.

Given that $\upsilon \sim -\frac{1}{2}$, we have essentially $z \propto \frac{T}{\beta} \propto A^{-1/2}$. We observed that the total amount of filamentous actin in cells increases with cell area, indicating that the parameter $\beta$ that determines the number of actin filaments must increase with cell area as well. It may scale as $\beta \propto \sqrt{A}$, which would mean that the total branching rate is proportional to the cell perimeter, or to the leading edge length, and could suggest perhaps that there is a molecular complex at the cell edge that regulates actin network assembly by activating Arp2/3[37]. If this were true, the membrane tension, *T*, would vary little with cell size. Another possibility is that $T \propto \sqrt{A}$. In that case, $\beta$ would increase essentially linearly with cell area; this scaling would also be a plausible biologically and suggest that filament branching is triggered by a membrane associated signal (rather than a leading-edge associated complex). Further research will be needed to address this distinction[38], and to verify the overall prediction of the model that $\frac{T}{\beta} \propto A^{-1/2}$.

**Front roughness and angular speed**

Angular speed anti-correlates strongly with cell aspect ratio (and, to a lesser extent, with all observables correlating with aspect ratio; Fig. S2). The model does not address the angular speed directly; qualitatively, cell turning is due to stochastic imbalances between different parts of the cell and spatial-temporal instabilities of the protrusion at the leading edge. Previously, we demonstrated that in cells with low aspect ratio (and lower levels of filamentous actin), the leading edge is much more unstable, causing more frequent and significant turns[8]. These instabilities were explained by a model similar to the model we use here. This connection between an unstable leading edge and less persistent directional motion is further reflected in the observed correlation between the front roughness measure (not directly addressed in the model, but which we believe to be indicative of the global order or disorder of the leading edge) and angular speed (Fig. S2).

Similarly, front roughness strongly anti-correlates with cell speed (Fig. S2). This could be explained by stochastic variations of the protrusion along the 'rough' leading edge, which are not synchronized as needed for rapid locomotion. The correlation of front roughness with actin monomer concentration could be explained if high actin monomer concentrations drive localized intermittent rapid growth of actin filaments. This probably contributes to greater observed variations of the cell speed for the lower aspect ratio cells.

**Filamentous actin concentration**

The average concentration of actin filaments in cells correlates with the actin density ratio, $D_{cs}$, and cell aspect ratio, *S*. This qualitatively agrees with the model, because when the total branching rate is elevated or the capping rate is lowered, or both, then the assembly of actin filaments is enhanced. At the same time, according to the model, *S* and $D_{cs}$ increase.

**Front-to-rear slope in actin filament density**

In smooth, high-aspect-ratio (i.e. "coherent") canoe-shaped cells, the actin filament density decreases from the leading edge toward the rear (Fig. S8b,c), indicating that filaments' appearance and growth are enhanced in a narrow band near the leading edge and disassemble uniformly throughout the lamellipodium [22,39]. (This observation is supported by kabiramide C staining of live cells). This front-to-rear decrease in actin filament density occurs along the entire leading edge. Indeed, the ratio of actin filament density near the leading edge to that farther rearward correlates with cell aspect ratio (Fig. S8d): it is largest in canoe-shaped cells with high aspect ratio; it becomes lower in cells with lower aspect ratios, and can even become less than one in the very decoherent, lowest aspect ratio cells. Though the model does not address these observations directly, they deserve some discussion. We explain these results as follows: when the overall branching rate is lower, cells for some reason are unable to focus most of the growing filaments at the cell edge, and new filaments grow to a greater extent throughout the lamellipodium (supported by kabiramide C staining, which is more uniform in cells with low aspect ratio). Thus, in low aspect ratio cells, additional assembly of actin filaments occurs throughout the lamellipodium and partially compensates for the disassembly of filaments created at the leading edge.

Note that in cells with low aspect ratios, the actin filament density at the leading edge is lower, but this density hardly decreases toward the rear, while in canoe-shaped cells, the filament density at the front is high, and decreases toward the rear. Thus, at the rear, the actin filament density probably varies much less than at the front. This supports our argument that membrane tension (which depends on the force needed to crush and push the actin network at the rear) varies little from cell to cell.

**Some other correlations**

Correlations that we did not comment on explicitly can be simply explained indirectly. For example, *R* correlates with $V_{cell}$ and $D_{cs}$ because all of these observables strongly correlate with *S*.

## 3. Model relation to data from individual cells through time

The data for individual cells' speed and shape as a function of time allowed us to characterize individual cell variability through time and compare it to the behavior of cell populations, most notably demonstrating the constancy of cell area within a given cell (Fig. 2a). We found that individual variability did not appreciably increase with time in the ranges observed (up to a few hours); thus individual cells do not appear to be ergodically exploring the phase space of the full population. In addition, these data provide further clues regarding the correlations between observables and the nature of the variability in the population data. First, we observe a strong correlation between the actin filament densities at the center and sides of the leading edge (Fig. S4a), for cells on the highly-ordered "coherent" side of the phenotypic spectrum. This indirectly supports one of the main modeling assumptions about the global regulation of filament branching in cells; if the total number of branching events per cell is regulated (as we assume in the model) than the actin density at different positions along the leading edge is expected to be correlated as observed, whereas if the branching was regulated locally such correlation would not be expected.

Second, the time-lapse data demonstrate that the actin filament density at the center of the leading edge correlates with aspect ratio, while the filament density at the side of the leading edge does not (data not shown). Roughly, this means, according to the model, that the membrane tension does not fluctuate in time much, while the parameter $\beta$ (or perhaps $\gamma$), and the amplitude of the actin profile with it, do. The actin filament density at the sides of the leading edge stays more or less constant to balance membrane tension, while the length of the front of the leading edge (and as area is constant, the cell's aspect ratio with it) fluctuates together with $D_c$ and cell speed. This is reflected in the larger temporal variation observed in $D_c$ relative to the variation in $D_s$, within the same cell as a function of time: $std(D_c(t))/mean(D_c(t), D_s(t)) = 0.22$; $std(D_s(t))/mean(D_c(t), D_s(t)) = 0.18$; the analysis was done for data points acquired at 10 second intervals over 200 seconds for 11 cells. Thus, significant fluctuations in either $\beta$, $\gamma$, or both, augmented by some variation in *T*, appear to explain the large variation in cell geometry and speed, both through time for individual cells, and across a population of cells.

## 4. Model limitations in explaining the data

An obvious limitation of the simple model presented here is that, for reasons of mathematical simplicity and more transparent comparison of model predictions with data, the complex cell shape is approximated simply by a bent rectangle. More sophisticated models based on differential equations lead to a more detailed description of the leading edge and sides of the cell[8], but quantitative comparison of the results of these models with experiments is not easy, and the biological conclusions are harder to decipher.

Moreover, the exact shape of the cell rear is beyond the current model framework. Implicitly, the model assumes that the rear edge is a circular arch of the same average radius as that of the leading edge, which is in fact not far from the truth. Additional simplifications of our model are the fact that we treat the lamellipodium as two-dimensional and that we ignore the effects of the cell body. However, these approximations are justifiable given the observations that the lamellipodium is flat and extremely thin[33,34] and that lamellipodial fragments of keratocytes (without a cell body) move in a manner essentially indistinguishable from whole cells[40,41].

Another problem in relating the model to experimental data is that the measured profile of filamentous actin density along the leading edge includes not only filaments growing and pushing the edge, but also presumably some filaments that are capped, stalled and/or buckled and thus not contributing to protrusion. The fraction of the latter is likely to be higher at the lamellipodial sides complicating quantitative interpretation of the actin density ratio. This problem is reflected in the deviation of the theoretical prediction from the experimentally measured relation $D_{cs}(S)$ for small values of $D_{cs}$ ($S$~1). The reason for this discrepancy is that the theory predicts only values $D_{cs} > 1$, and in low aspect ratio cells, where the actin filament distribution along the leading edge is relatively flat, there is probably a large fraction of capped, buckled and stalled filaments at the sides so the error in interpreting $D_{cs}$ becomes larger.

The model prediction also becomes poor for very large values of $D_{cs}$ ($S$>1.6), albeit for a different reason. Cells characterized by high values of $D_{cs}$ are canoe-like, with an aspect ratio much greater than 1, which means that their widths, $x$, are large, while their lengths, $y$, are very small. It is plausible then that the actin network does not have enough time to disassemble during its transit from cell front to rear, causing an increase in membrane tension. Mathematically, this would lead to a non-linear correction for cell shapes characterized by high values of $D_{cs}$. Explicitly including such non-linearity into the model at this point would only complicate matters without adding biological insight.

Finally, there are many processes that are each of secondary importance to the overall cell shape for keratocytes, yet together they introduce additional "noise" in cell behavior and errors in the theory-experiment relation. Among those are corrections to the sides' shape due to the myosin-powered centripetal actin network flow, retraction fibers at the cell rear, and potential contribution of the adhesions to membrane tension and protrusion.

Note also that the situation in other cell types is likely more complicated. While other well-characterized motile cells such as fibroblasts and neutrophils rely on the same molecular components and mechanisms involved in keratocyte motility[9,42,43], keratocyte shapes are considerably simpler and far more stereotyped. In particular, other cell types typically have more variable shapes, both across the population and in individual cells through time. Unlike keratocytes, more complex cells are likely to exhibit significant hysteresis (history-dependence) in shape – for example, the shape of a fibroblast at any given time is likely to be a reflection of that cell's immediate past history of protrusions

and retractions, and is not likely to reconstitute in the same configuration after actin network collapse as do keratocytes (Fig. 2c-e).

## *5. Molecular perturbation experiments and their theoretical interpretation*

To further investigate the role of various molecular processes in determining cell shape, we targeted specific components of the cytoskeleton in live cells with pharmacological agents. The agents employed included several actin drugs: cytochalasin D, which caps actin filaments and affects nucleotide hydrolysis on monomers[44]; latrunculin, which sequesters actin monomers[45]; and jasplakinolide, which stabilizes actin filaments and slows depolymerization[46]. We also employed two compounds that target myosin: blebbistatin, which is a specific myosin II inhibitor[47]; and calyculin A, which enhances myosin II activity by inhibiting a myosin light chain phosphatase[48]. All these treatments elicited statistically significant morphological changes (Fig. S1a), but their extent was rather small, as illustrated by the similarity of the mean shape of each perturbed population to that of the untreated cells (Fig. S1b). In particular, the natural shape variation in the population (Fig. 1) was substantially larger than the shifts induced by any of these perturbations (Fig. S1). Furthermore, the phase space of cell shapes under these perturbations was nearly identical to that spanned by the population of unperturbed cells. Specifically, the first two shape modes were essentially unchanged by these molecular perturbations (Fig. S1b), and in all treatments but jasplakinolide, modes three and four remained intact (data not shown). Note that concentrations of these drugs higher than those we employed typically lead to "catastrophic" phenotypes with no movement and no lamellipodium. However, as long as keratocytes are moving and possess a lamellipodium, the spectrum of cell shapes remains largely unchanged.

Two parameters in our simple model describe an individual cell, and are thus of use in relating the effects of these perturbations to their molecular mechanisms: area, $A$, and the lumped parameter $z = T\gamma / \left( f_{stall}\beta \right)$, where $T$ is the membrane tension, $\gamma$ is the capping rate, $f_{stall}$ is the per-filament stall force, and $\beta$ is the branching rate per cell per second. The outcome of the model with regards to cell speed also depends on the value for the cellular actin monomer concentration (see eq. (20) above), so we use $G$ as an additional parameter (we do not have experimental data on how the perturbations change the actin monomer concentration). The distribution of cell areas of perturbed cells does not change much compared to untreated cells (Fig. S1). Therefore, we attempt to explain the observed changes in cell geometry and speed quantitatively by changes in the parameters $z$ and $G$. Some perturbations show a change in $z$ that is relatively straightforward to explain; however other perturbations may either affect more than one of the parameters that go into the lumped parameter $z$ (and since the relative magnitude of these changes is hard to anticipate, $z$ can go either up or down), or require the invocation of compensatory mechanisms for a satisfactory explanation.

We focus here on the effect these agents have on (i) aspect ratio, (ii) lamellipodial radius, (iii) cell speed. Other observables, such as cell perimeter, actin ratio, roughness, etc. are logically connected to these main ones. The shape of the cell rear and its reaction to perturbations are not discussed here and will be addressed in future work. Note that we will discuss the perturbation-induced changes qualitatively, as there is no quantitative information on the molecular effects of these perturbations. In order to consider these three observables, the following formulae derived above are used:

$$z = \frac{T\gamma}{f_{stall}\beta}, S \approx 10\left(1-(zL)\right), R \sim \sqrt{\left((zL)^{-w}-1\right)A}, V \sim G\left(1-(zL)^{w}\right) \qquad (21)$$

The formula for S is a linear approximation to equation (13); also, recall that $L \approx 3\sqrt{A}$, and so L does not change significantly upon perturbations.

*Cytochalasin* The measured changes can be explained neatly by the model: effectively, cytochalasin increases the capping rate, $\gamma$ [44], so, according to (21), *z* goes up, and $S, R, V$ all decrease, as observed.

*Blebbistatin* These effects are also very easy to understand: according to our model, myosin-powered contraction assists actin filament disassembly at the rear of the cell. Blebbistatin inhibits myosin contraction[47] and without this assistance[7], tension *T* is likely to increase as the membrane encounters a greater resistance of a more intact actin network at the rear. Thus, *z* goes up, and $S, R, V$ all go down, as observed.

*Calyculin* The effects of this treatment can be explained as follows. Calyculin brings the tension *T* down, likely by increasing the centripetal actin flow[48]. However, it may also drive actin filament assembly down by mechanically sliding and/or straining actin filaments and inhibiting branching, so if $\beta$ decreases to a greater extent than *T*, then *z* increases, and $S, R$ decrease, as observed. At the same time, calyculin may indirectly enhance actin network disassembly by making myosin break actin filaments more vigorously. This could significantly increase the actin monomer concentration, and this increase could overcome the decrease of the *z*-related factor in the formula for cell speed, leading to increased speed as observed. Also, higher actin monomer concentration could elevate the branching rate, if Arp2/3-mediated branching depends on the rate of monomer addition.

Note also, that the perturbations of myosin contraction (blebbistatin and calyculin) are the only ones significantly affecting the angular speed of cells (Fig. S1). While the model does not address this directly, we hypothesize that this is related to the subtle balance of retractions of the right and left rear corners of the cell being dependent on myosin-generated centripetal actin flow.

*Latrunculin* Latrunculin sequesters actin monomers[45], and since Arp2/3-mediated branching depends on the rate of actin monomer addition[49], it could thereby decrease the branching rate, $\beta$. This would increase parameter *z* and decrease *S* and *R*, as observed. The observed decrease in cell speed is easy to explain because the actin monomer concentration likely decreases due to monomer sequestration.

*Jasplakinolide* The effects of this drug are not easy to explain, but the following mechanism is plausible. Jasplakinolide stabilizes actin filaments[46], so it probably enhances branching and increases parameter $\beta$ , despite inverse effect of the lower actin monomer concentration. *T* is also likely to increase, but maybe not to the same extent, so as a result parameter *z* decreases slightly, so *S* increases. It is easy to explain the decrease in cell speed: actin filaments are stabilized, so the actin monomer concentration is reduced resulting in lower speed (despite the slight increase of the *z*-related factor).

## *6. Ruling out other potential models*

Our quantitative model for the fronts/sides of the cell is based on the hypothesis that protrusion is force-limited, and that the actin filament density along the leading edge is graded. Thus, the filaments at the sides are stalled because they are fewer in number and collectively unable to protrude against the membrane tension, while the numerous filaments at the front together push the leading edge effectively. The model for the rear edge of the cell, which is much less explicit or quantitative at present, is based on the idea that the membrane tension pushes forward debris of the actin network that is likely largely disassembled at the rear. Here, we discuss possible alternative hypotheses and their relations to the data. These alternatives include:
a) Global angular actin network architecture
b) Graded actin monomer concentration
c) 'Central organizer' of the cell shape, i.e., MTOC
d) Myosin-powered graded centripetal flow
e) Pre-set leading edge length
f) Depolymerization 'clock'
Hypotheses (a-d) are illustrated schematically in Fig. S3. A role for microtubules is ruled out by the lack of a shape phenotype under nocodazole treatment (data not shown) and the observation that microtubules are not required for keratocyte motility[40]. Likewise, a hypothetical "morphogen field" or other central organizing principle (hypothesis (c)) fail to explain the observed correlations among different morphological characteristics (Fig. 2b). The discussion below details how the extensive dataset acquired in this work allows us to test and refute the other alternative hypothesis mentioned above.

It is important to note here that while our model explains the main trends in the data, we do not rule out some additional contributions from other mechanisms including those listed above. The arguments given below explain why the above mechanisms cannot by themselves be the main factor determining cell shape, and show how such mechanisms would lead to predictions that are inconsistent with the data. However, more subtle contributions, particularly for the more extreme shapes, may well occur. As an example, it is possible that the depolymerization clock mechanism sets a lower limit on cell length (y) and may affect the shape of cells if their width approaches this limit.

**Global angular actin network architecture**. It is possible, in principle, that actin filaments are oriented on average in the direction of protrusion globally everywhere in the cell, rather than locally normal to the cell edge (Fig. S3a). According to this idea and the branching geometry, only roughly half of the filaments would be pushing at the cell sides relative to the front, so that the sides could be stalled while the front protrudes forward. Graded actin filament density would be irrelevant, and this hypothesis would explain the geometry of the cells with relatively flat actin filament density profiles along their leading edges.

*Arguments against this hypothesis*: A flat actin density profile would result in a very flat leading edge, with an enormous lamellipodial radius. This hypothesis would certainly not predict the observed correlation of radius with area and aspect ratio, which requires graded actin filament density profile. Also, it fails to predict the observed relation between the actin density ratio and aspect ratio.

**Graded actin monomer concentration**. If most actin filament depolymerization took place in the cell body, then actin monomer diffusion from the cell body across the lamellipodium and 'consumption' along the leading edge would lead to roughly radial downward gradient of actin monomer density with its center at the cell body. In this scenario, the lamellipodial sides, to which the distance from the cell body is longest, would have lower actin monomer concentration (Fig. S3b). At the lamellipodial front, which is closest to the cell body, the monomer concentration would be higher. In canoe-shaped cells, if protrusion was limited by actin monomer availability, protrusion at the sides would be slowed down due to lower monomer concentration there, and the resulting graded protrusion could explain cell shape.

*Arguments against this hypothesis*: First, there is experimental evidence that depolymerization is distributed laterally more or less uniformly in the cell[24]. It is possible that myosin could move filamentous actin toward the cell center and thus concentrate disassembly there; however, myosin inhibition, which therefore forces depolymerization to occur along the whole rear edge of the cell, produces no dramatic effect on cell shapes (Fig. 1c). Second, our data indicate that actin monomer concentration anti-correlates with aspect ratio (in fixed cells), which in turn correlates with cell speed (in live cells), arguing against actin monomer-limited protrusion. Third, this model could not explain the shape of low aspect ratio cells where the lamellipodial sides are as close to the cell body as the lamellipodial front. Finally, this model would predict anti-correlation of cell speed and cell area, which is not observed. We can similarly rule out various "morphogen field" hypotheses, which propose that reaction-diffusion of some regulatory molecule results in a concentration gradient of that molecule, establishing spatial cues that determine cell shape[50].

**Myosin graded inward flow**: Myosin-powered centripetal flow of the lamellipodial actin network is graded[24,25], so that the flow in the laboratory frame of reference is slow at the lamellipodial front and faster at the sides and rear. According to this hypothesis, even if actin filament growth rate was uniform around the cell boundary, this growth could be

balanced by the inward actin network flow at the sides of the lamellipodium and overcome at the rear, while only slightly perturbed at the front (Fig. S3d).

*Arguments against this hypothesis*: First, actin network flow maps obtained in our lab[7] show almost no flow at the lamellipodial sides near the front of the cell. More importantly, this hypothesis would predict that blebbistatin (calyculin) inhibiting (strengthening) myosin would cause significant changes in cell geometry and speed, which are not observed. More subtly, some of our observations, such as the correlations between aspect ratio and cell speed, and between lamellipodial radius and area, are hard to explain quantitatively in the framework of this hypothesis. We emphasize though that none of these observations rule out the possibility for myosin-powered graded inward flow to play an important role in shape determination of other motile cell types.

**Regulated leading edge length**: One very hypothetical possibility is that a linear supra-molecular structure, the length of which is determined by some pathway(s) that are not part of the self-organizing mechanisms that we discuss in this paper[51], defines the length of the leading edge, *x*. Then, given a constant cell area, the aspect ratio would be uniquely defined.

*Arguments against this hypothesis*: It would be hard to explain why aspect ratio correlates with cell area, why speed correlates with aspect ratio, and why lamellipodial radius correlates with cell area; many more correlations would require very elaborate assumptions to explain them.

**Depolymerization clock**: This hypothesis states that the distance between the front and the rear of the lamellipodium, *y*, is determined by the time $\tau$ needed for disassembly of the actin network: $y = V_{cell}\tau$ .

*Arguments against this hypothesis*: It would predict a correlation of cell speed with the front-to-rear distance, which is not observed. Also, this hypothesis would predict a much stronger correlation between aspect ratio and area than observed (*y* would be more or less constant for all cells, so *x* would increase significantly as *A* grows). However, the depolymerization clock could be a crucial mechanism determining the rear edge shape in the sub-population of the cells characterized by small *y*, as discussed above.

# Supplementary methods

**Cell culture, fixation and microscopy.**
To obtain additional information about the distributions of both actin monomers and actin filaments and their correlations with cell morphology, the population-based analysis described in the main text for live cells (Figures 1,2) was repeated for a population of fixed keratocytes co-stained for actin monomers and filamentous actin. All treatments prior to fixation were identical to the live cell experiments described in the main text. Briefly, keratocytes were cultured from the scales of the Central American cichlid *Hypsophrys nicaraguensis* as described previously[8]. Keratocyte sheets from one day old

cultures were disaggregated by incubating in 85% PBS and 2.5 mM EGTA, pH 7.4, for 5 min, followed by incubation in normal media for an additional ~1.5–2 hours. Cells were fixed with 4% Formaldeyde as described elsewhere[52] followed by co-staining of filamentous actin with Rhodamine-phalloidin (Cytoskeleton Inc.) and actin monomers with FITC-DNAseI (Molecular Probes). We attempted to keep the concentration and duration of staining constant, but still we observed considerable variation of staining intensities between different coverslips. To compare relative amounts of actin between cells on different coverslips we employed a coverslip based normalization scheme described below. In addition, comparison of the fixed cell data set with the live cell one, revealed that the fixation process introduced moderate, yet statistically significant, changes in cell shape (Fig. S1).

Images of fixed cells were collected with a microscope (Axioplan 2; Carl Zeiss MicroImaging, Inc.) using a 63× NA 1.4 oil plan-Apochromat objective (Carl Zeiss MicroImaging, Inc.). Images were collected with a cooled back-thinned CCD camera (MicroMax 512BFT; Princeton Instruments) with a 2× optovar attached using MetaMorph software version 6 (Molecular Devices). For each coverslip, ~10–35 polarized cells were randomly chosen for imaging.

Filamentous and monomeric actin concentrations in fixed cells were measured by phalloidin and DNAseI staining intensities, respectively. The total integrated intensity within the cell outline was divided by the cell area to provide a crude measure of concentration. These values varied greatly between coverslips because of differential staining; thus the values were re-centered to set the median of each coverslip to 1. (Values were not re-scaled: though the distributions of values for each coverslip had different centers, the spreads were comparable and thus did not warrant correction.)

**Algorithm 1: Alignment of two polygons with weighted landmark**

It is simple to find the rotation and translation that optimally align two collections of points via a closed-form procedure that minimizes the sum of squared distances between corresponding points known as Procrustes analysis[53]. The complexity here is that the exact point correspondences between cell shapes represented as polygons are not known: for a 200-point polygon, there are 200 possible different point orderings for a given winding direction (clockwise or counterclockwise). A brute-force method to align two 200-point polygons would simply be to apply the Procustes method 200 times, and take the alignment with the smallest squared error as optimal. We obtain a significant speedup over this approach by trying only eight possible orderings for each direction and "hill-climbing" to a local optimum from each of those starting points. This procedure is not guaranteed to find the global optimum, but we have found it very reliable on the shapes used in this work. To further help the alignment of keratocyte shapes, we have found it helpful to define an approximate "cell body position," determined either manually or from the bright spot of fluorescence produced by the cell body, as a landmark to be aligned in the Procrustes procedure. (This landmark is of course not re-ordered with other points, as a general correspondence in the cell body positions is assumed across all cells.) The Procrustes method allows for different points to be differently weighted, and we have

found that assigning a weight of 0.3 to the point at the center of the cell body, and a weight of 0.7 shared among polygon points allows for good alignment. Note that while in some cases it might be reasonable to allow for reflections of shapes if that provides a smaller squared error term, it is not reasonable to do so for keratocytes, as these cells have distinct top and bottom surfaces, which reflecting would implicitly disregard.

**Algorithm 2: Mutual alignment of a population of shapes**
This method has been previously described[54]; briefly, an expectation-maximization procedure is used to simultaneously estimate the mean cell shape in the population and align all cells to that mean. As an initialization step, the polygons are roughly aligned along their long axes and ordered winding counterclockwise from the rearmost point. Then, the mean of the (unaligned) population is calculated, and each cell is aligned to that mean via Algorithm 1. The mean is re-computed from the newly aligned cells, which are then aligned to the new mean, until no cells change their position (above a certain low threshold). At this point, the cells are considered aligned.

## Supplementary references


1 Grimm, H. P., Verkhovsky, A. B., Mogilner, A., and Meister, J. J., Analysis of actin dynamics at the leading edge of crawling cells: implications for the shape of keratocyte lamellipodia. *Eur Biophys J* **32** (6), 563 (2003).

2 Schaus, T. E. and Borisy, G., Performance of a population of independent filaments in lamellipodial protrusion. *Biophys J (in press)* (2007).

3 Schaus, T. E., Taylor, E. W., and Borisy, G. G., Self-organization of actin filament orientation in the dendritic-nucleation/array-treadmilling model. *Proc Natl Acad Sci U S A* **104** (17), 7086 (2007).

4 Raucher, D. and Sheetz, M. P., Cell spreading and lamellipodial extension rate is regulated by membrane tension. *J Cell Biol* **148** (1), 127 (2000).

5 Prass, M., Jacobson, K., Mogilner, A., and Radmacher, M., Direct measurement of the lamellipodial protrusive force in a migrating cell. *J Cell Biol* **174** (6), 767 (2006).

6 Lee, J., Ishihara, A., Theriot, J. A., and Jacobson, K., Principles of locomotion for simple-shaped cells. *Nature* **362** (6416), 167 (1993).

7 Wilson, C. A. et al., Myosin II contributes to rear retraction by promoting F-actin turnover in motile cells. *Submitted* (2008).

8 Lacayo, C. I. et al., Emergence of Large-Scale Cell Morphology and Movement from Local Actin Filament Growth Dynamics. *PLoS Biol* **5** (9), e233 (2007).

9 Lee, J. and Jacobson, K., The composition and dynamics of cell-substratum adhesions in locomoting fish keratocytes. *J Cell Sci* **110 ( Pt 22)**, 2833 (1997).

10 Pollard, T. D., Blanchoin, L., and Mullins, R. D., Molecular mechanisms controlling actin filament dynamics in nonmuscle cells. *Annu Rev Biophys Biomol Struct* **29**, 545 (2000).

11 Mogilner, A., On the edge: modeling protrusion. *Curr Opin Cell Biol* **18** (1), 32 (2006).

12 Kovar, D. R. and Pollard, T. D., Insertional assembly of actin filament barbed ends in association with formins produces piconewton forces. *Proc Natl Acad Sci U S A* **101** (41), 14725 (2004).

13 Footer, M. J., Kerssemakers, J. W., Theriot, J. A., and Dogterom, M., Direct measurement of force generation by actin filament polymerization using an optical trap. *Proc Natl Acad Sci U S A* **104** (7), 2181 (2007).

14 Chaudhuri, O., Parekh, S. H., and Fletcher, D. A., Reversible stress softening of actin networks. *Nature* **445** (7125), 295 (2007).

15 Bear, J. E. et al., Antagonism between Ena/VASP proteins and actin filament capping regulates fibroblast motility. *Cell* **109** (4), 509 (2002).

16 Mogilner, A. and Oster, G., Cell motility driven by actin polymerization. *Biophys J* **71** (6), 3030 (1996).

17 Carlsson, A. E., Growth velocities of branched actin networks. *Biophys J* **84** (5), 2907 (2003).

18 Peskin, C. S. and Oster, G. F., Force production by depolymerizing microtubules: load-velocity curves and run-pause statistics. *Biophys J* **69** (6), 2268 (1995).

19 Coppin, C. M., Pierce, D. W., Hsu, L., and Vale, R. D., The load dependence of kinesin's mechanical cycle. *Proc Natl Acad Sci U S A* **94** (16), 8539 (1997).

20 Marcy, Y., Prost, J., Carlier, M. F., and Sykes, C., Forces generated during actin-based propulsion: a direct measurement by micromanipulation. *Proc Natl Acad Sci U S A* **101** (16), 5992 (2004).

21 Parekh, S. H., Chaudhuri, O., Theriot, J. A., and Fletcher, D. A., Loading history determines the velocity of actin-network growth. *Nat Cell Biol* **7** (12), 1219 (2005).

22 Theriot, J. A. and Mitchison, T. J., Actin microfilament dynamics in locomoting cells. *Nature* **352** (6331), 126 (1991).

23 Jurado, C., Haserick, J. R., and Lee, J., Slipping or gripping? Fluorescent speckle microscopy in fish keratocytes reveals two different mechanisms for generating a retrograde flow of actin. *Mol Biol Cell* **16** (2), 507 (2005).

24 Schaub, S. et al., Comparative Maps of Motion and Assembly of Filamentous Actin and Myosin II in Migrating Cells. *Mol Biol Cell* **18** (10), 3723 (2007).

25 Vallotton, P. et al., Tracking retrograde flow in keratocytes: news from the front. *Mol Biol Cell* **16** (3), 1223 (2005).

26 Cevc, G. and Marsh, D., *Phospholipid Bilayers: Physical Principles and Models*. (Willey, New York, 1987).

27 Lipowsky, R. and Sackmann, E., *Structure and Dynamics of Membranes.* (Elsevier, Amsterdam, 1995).

28 Sheetz, M. P., Sable, J. E., and Dobereiner, H. G., Continuous membrane-cytoskeleton adhesion requires continuous accommodation to lipid and cytoskeleton dynamics. *Annu Rev Biophys Biomol Struct* **35**, 417 (2006).

29 Waugh, R. E., Surface viscosity measurements from large bilayer vesicle tether formation. II. Experiments. *Biophys J* **38** (1), 29 (1982).

30 Waugh, R. E., Surface viscosity measurements from large bilayer vesicle tether formation. I. Analysis. *Biophys J* **38** (1), 19 (1982).

31 Kucik, D. F., Elson, E. L., and Sheetz, M. P., Cell migration does not produce membrane flow. *J Cell Biol* **111** (4), 1617 (1990).

32 Evans, E. and Skalak, R., *Mechanics and Thermodynmics of Biomembranes*. (CRC, Boca Raton, Florida, 1980).

33 Abraham, V. C., Krishnamurthi, V., Taylor, D. L., and Lanni, F., The actin-based nanomachine at the leading edge of migrating cells. *Biophys J* **77** (3), 1721 (1999).

34 Euteneuer, U. and Schliwa, M., The function of microtubules in directional cell movement. *Ann N Y Acad Sci* **466**, 867 (1986).

35 Dunn, G. A. and Zicha, D., Dynamics of fibroblast spreading. *J Cell Sci* **108 ( Pt 3)**, 1239 (1995).

36 Raucher, D. and Sheetz, M. P., Characteristics of a membrane reservoir buffering membrane tension. *Biophys J* **77** (4), 1992 (1999).

37 Pollard, T. D. and Borisy, G. G., Cellular motility driven by assembly and disassembly of actin filaments. *Cell* **112** (4), 453 (2003).

38 Iwasa, J. H. and Mullins, R. D., Spatial and temporal relationships between actin-filament nucleation, capping, and disassembly. *Curr Biol* **17** (5), 395 (2007).

39 Watanabe, N. and Mitchison, T. J., Single-molecule speckle analysis of actin filament turnover in lamellipodia. *Science* **295** (5557), 1083 (2002).

40 Euteneuer, U. and Schliwa, M., Persistent, directional motility of cells and cytoplasmic fragments in the absence of microtubules. *Nature* **310** (5972), 58 (1984).

41 Verkhovsky, A. B., Svitkina, T. M., and Borisy, G. G., Self-polarization and directional motility of cytoplasm. *Curr Biol* **9** (1), 11 (1999).

42 Svitkina, T. M. and Borisy, G. G., Arp2/3 complex and actin depolymerizing factor/cofilin in dendritic organization and treadmilling of actin filament array in lamellipodia. *J Cell Biol* **145** (5), 1009 (1999).

43 Svitkina, T. M., Verkhovsky, A. B., McQuade, K. M., and Borisy, G. G., Analysis of the actin-myosin II system in fish epidermal keratocytes: mechanism of cell body translocation. *J Cell Biol* **139** (2), 397 (1997).

44 Cooper, J. A., Effects of cytochalasin and phalloidin on actin. *J Cell Biol* **105** (4), 1473 (1987).

45 Coue, M., Brenner, S. L., Spector, I., and Korn, E. D., Inhibition of actin polymerization by latrunculin A. *FEBS Lett* **213** (2), 316 (1987).

46 Bubb, M. R. et al., Jasplakinolide, a cytotoxic natural product, induces actin polymerization and competitively inhibits the binding of phalloidin to F-actin. *J Biol Chem* **269** (21), 14869 (1994).

47 Straight, A. F. et al., Dissecting temporal and spatial control of cytokinesis with a myosin II Inhibitor. *Science* **299** (5613), 1743 (2003).

48 Henson, J. H. et al., Actin-based centripetal flow: phosphatase inhibition by calyculin-A alters flow pattern, actin organization, and actomyosin distribution. *Cell Motil Cytoskeleton* **56** (4), 252 (2003).

49 Mullins, R. D., Heuser, J. A., and Pollard, T. D., The interaction of Arp2/3 complex with actin: nucleation, high affinity pointed end capping, and formation of branching networks of filaments. *Proc Natl Acad Sci U S A* **95** (11), 6181 (1998).

50 Meyers, J., Craig, J., and Odde, D. J., Potential for control of signaling pathways via cell size and shape. *Curr Biol* **16** (17), 1685 (2006).

51 Marshall, W. F., Cellular length control systems. *Annu Rev Cell Dev Biol* **20**, 677 (2004).

52 Yam, P. T. and Theriot, J. A., Repeated cycles of rapid actin assembly and disassembly on epithelial cell phagosomes. *Mol Biol Cell* **15** (12), 5647 (2004).

53 Goodall, C., Procrustes methods in statistical analysis of shape. *Journal Royal Statistical Society Series B- Methodological* **53** (2), 285 (1991).

54 Pincus, Z. and Theriot, J. A., Comparison of quantitative methods for cell-shape analysis. *J Microsc* **227** (Pt 2), 140 (2007).

**a**

| | Shape Mode 1 | Shape Mode 2 | Area ($\mu m^2$) | Aspect Ratio | Front Radius ($\mu m$) | Front Roughness | Speed ($\mu m$/sec) | Angular Speed (degrees/sec) | |
|---|---|---|---|---|---|---|---|---|---|
| Untreated Live Cells | **0 ± 1** | **0 ± 1** | **403 ± 164** | **1.86 ± 0.46** | **23.6 ± 12.2** | **1.96 ± 1.68** | **0.18 ± 0.07** | **0.29 ± 0.30** | n=400 |
| Stained (Kabiramide C) | **0.09 ± 0.91** | **−0.24 ± 0.97** | **428 ± 153** | **1.81 ± 0.46** | 23.6 ± 12.0 | 2.06 ± 1.51 | **0.19 ± 008** | **0.36 ± 0.44** | n=295 |
| Fixed (4% Formaldehyde) | 0.05 ± 0.80 | **−0.42 ± 0.95** | **427 ± 145** | **1.74 ± 0.39** | **21.6 ± 9.3** | **2.23 ± 1.54** | NA | NA | n=201 |
| Latrunculin 10 nM sequesters actin monomer | **0.09 ± 0.87** | **−0.18 ± 0.874** | **426 ± 156** | **1.79 ± 0.34** | **21.0 ± 7.6** | **1.79 ± 0.75** | **0.13 ± 0.06** | 0.33 ± 0.51 | n=144 |
| Cytochalasin D 1 µM caps actin filaments affects nucleotide hydrolysis | −0.09 ± 0.84 | **−0.46 ± 0.71** | 410 ± 154 | **1.63 ± 0.25** | **18.8 ± 5.9** | 2.02 ± 1.14 | **0.12 ± 0.06** | 0.36 ± 0.53 | n=77 |
| Jasplakinolide 500 nM stabilizes actin filaments | **0.16 ± 0.95** | **0.15 ± 0.88** | 422 ± 142 | **1.95 ± 0.42** | 24.7 ± 10.1 | **1.65 ± 0.96** | **0.15 ± 0.05** | 0.34 ± 0.50 | n=85 |
| Blebbistatin 50 µM inhibits myosin II | **−0.18 ± 0.89** | −0.10 ± 0.91 | **380± 148** | **1.71 ± 0.32** | **18.7 ± 7.1** | **2.15 ± 0.87** | **0.12 ± 0.06** | **0.19 ± 0.24** | n=112 |
| Calyculin A 25 nM enhances myosin II activity | **0.14 ± 0.68** | −0.09 ± 0.81 | **427 ± 127** | 1.84± 0.31 | **22.2 ± 6.5** | **1.74 ± 0.81** | **0.27 ± 0.09** | **0.45 ± 0.89** | n=133 |

**mean ± standard deviation**

**significant decrease from untreated** | no change from untreated | **significant increase from untreated**

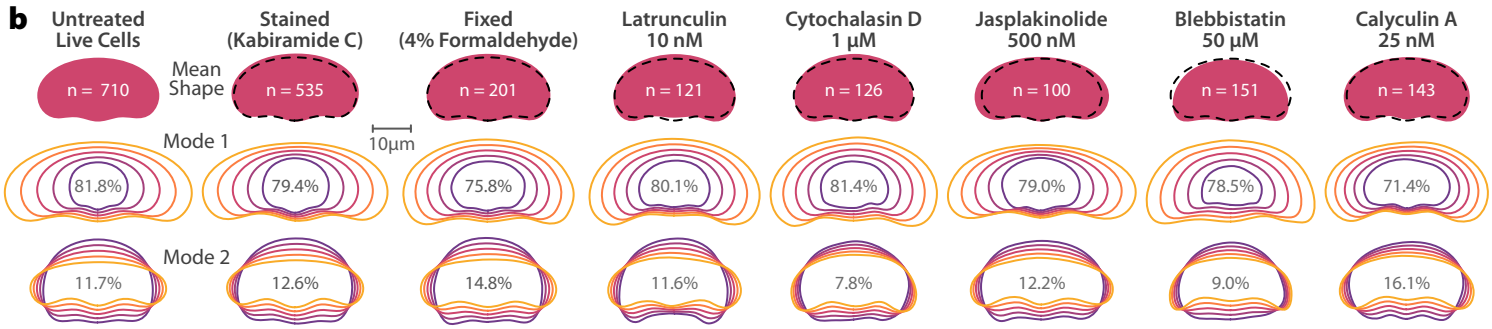


**Figure S1 – Molecular perturbations shift cell populations in distinct but subtle manners.**
(a) Shown are the mean ± standard deviation of each of the measured properties for cell populations under different molecular perturbations. Significant changes in means ($p<0.05$; determined from a bootstrap confidence interval on the difference in means) are colored and shown in bold face. At the right of the table a dendrogram shows the relationship between the different perturbations as determined by average-linkage hierarchical clustering based on the Mahalanobis distance between the mean measurement vector for each perturbation.
(b) Molecular perturbations have only a modest effect on cell shape. The top row shows the mean shapes of populations of cells treated with different agents at least 10 min before imaging; the mean shape of the unperturbed population is superimposed (dashed line). In the lower rows, the first and second principal modes of shape variation in these populations are illustrated by superimposition of the mean shape and shapes at one and two standard deviations away from that mean along each mode.

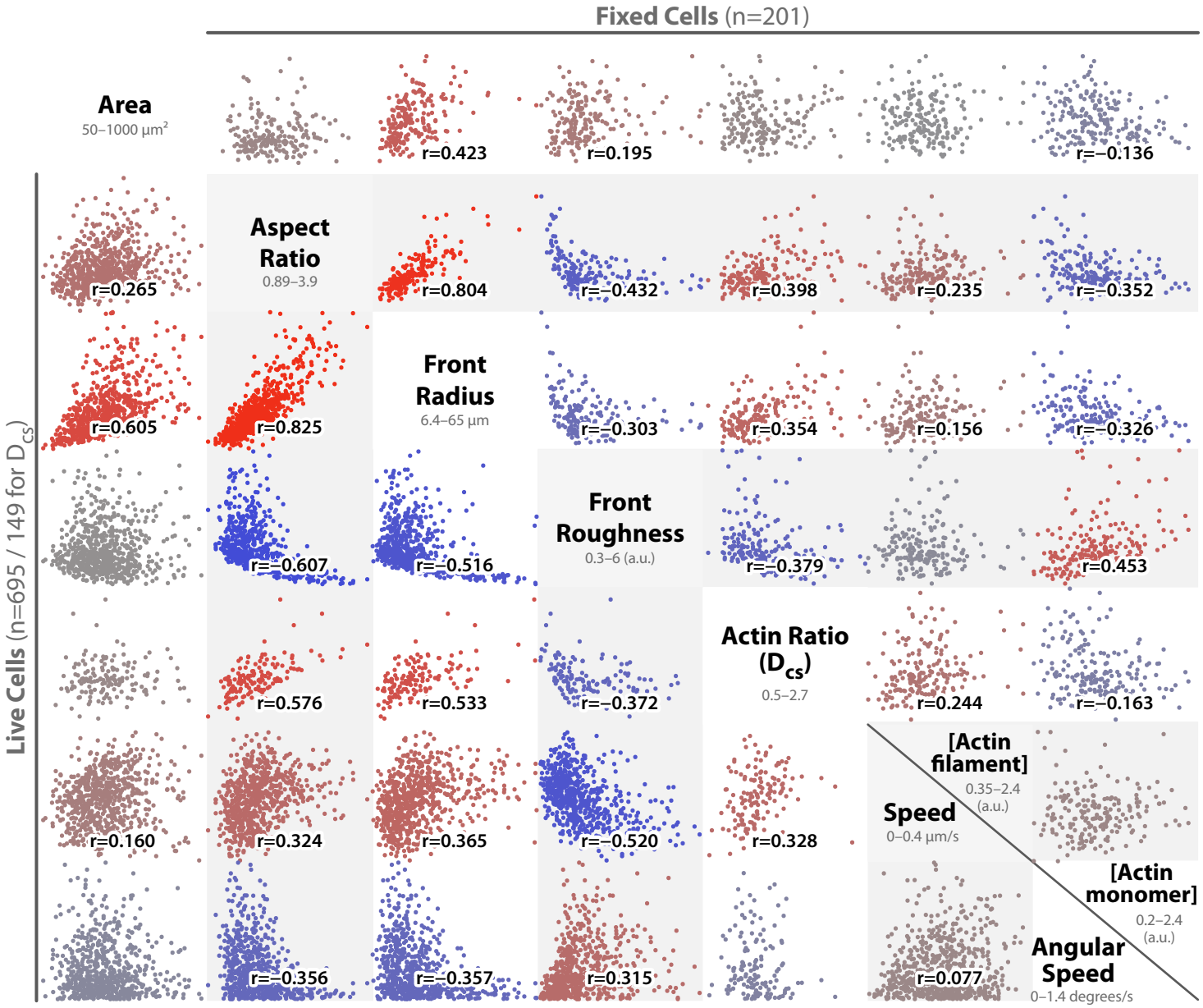


**Figure S2 – Correlations between measurements reveal a phenotypic continuum.**
Pairwise correlations between measurements gathered from live and fixed keratocyte populations are presented. Scatter-plots of the various measures (in pairwise combinations) are shown; the plot's row corresponds to the measurement plotted on the x-axis, and the column indicates the measurement on the y-axis. Measurements are named on the diagonal, and the range of values plotted is shown. Measurements of the fixed population are shown in the upper-right triangle, and the live population in the lower-left triangle. Each data point in the scatter-plots represents an individual cell. Plots are colored by the Spearman rank-order correlation score, which is comparable to Pearson's r statistic, but is more robust to outliers, with negative correlations in shades of blue and positive correlations in shades of red. Numeric correlation values are shown for data that have values significantly different from zero ($p < 0.05$; determined from a bootstrap confidence interval on the Spearman score). A small number of outliers were excluded, as follows. Area: 1 (live); front radius: 7 (live), 1 (fixed); front roughness: 21 (live), 7 (fixed); actin ratio: 5 (fixed); angular speed: 8 (live); actin filament concentration: 2 (fixed); actin monomer concentration: 1 (fixed).

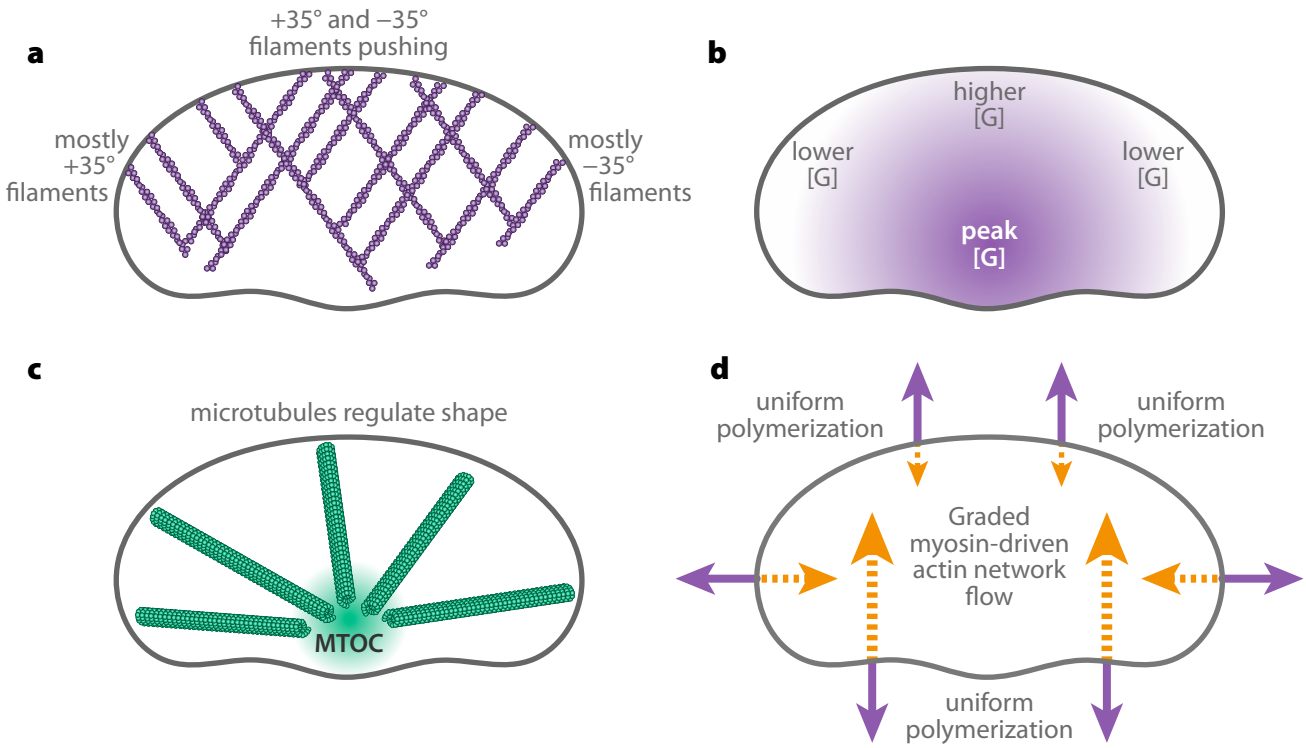


**Figure S3 – Schematic illustrations of alternative models for possible mechanisms of cell shape determination in keratocytes.**
(a) The actin network is organized so that filaments are oriented on average in the direction of protrusion (rather than locally normal to the cell edge) everywhere in the cell. Only roughly half of the filaments would be pushing at the cell sides relative to the front, so that the sides could be stalled while the front is protruding. (b) A gradient of actin monomer concentration centered at cell body leads to graded protrusion rate due to differences in local actin monomer concentration; monomer concentration at the sides is lower (since they are further away from the cell body) leading to slower protrusion there and limiting the ability of the cell sides to extend further. (c) Microtubules (with the microtubule-organizing center (MTOC) localized at the cell body) play a central role in shape determination. (d) Myosin-powered graded actin network centripetal flow balances uniform network growth to yield the observed graded extension; at the front myosin-driven flow is small and protrusion is dominated by polymerization, at the sides myosin-driven flow cancels polymerization to yield no net protrusion, and finally at the rear myosin-driven flow dominates leading to retraction of the cell rear.

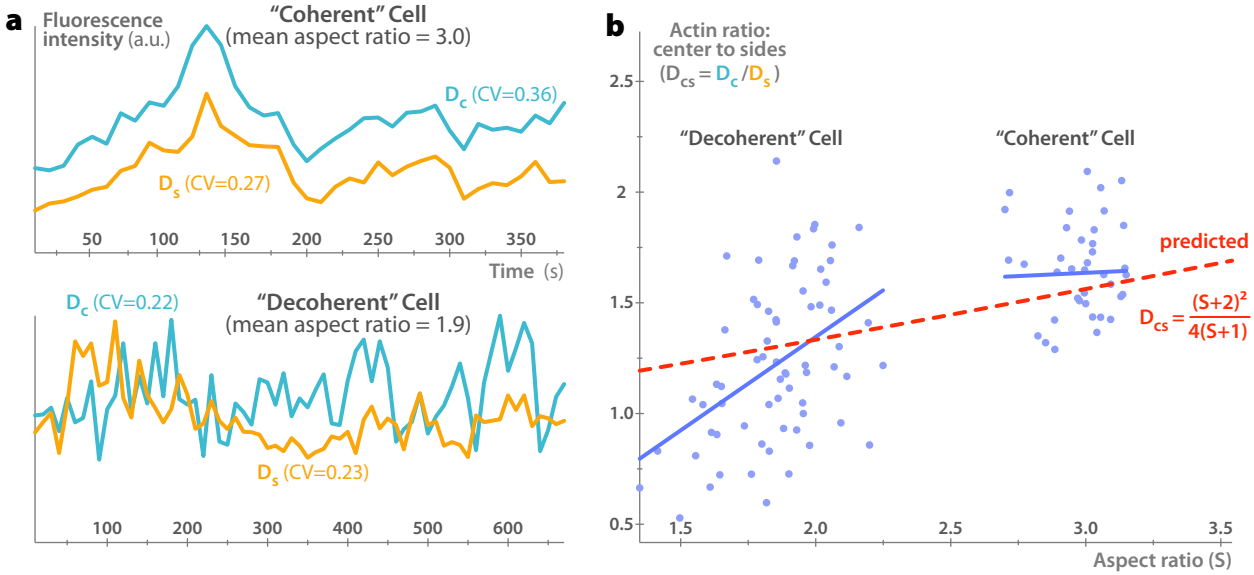


**Figure S4 – Data from individual cells through time.**
Data from a "coherent" cell (see Supplementary Movie 2) and a "decoherent" cell (see Supplementary Movie 3) stained with kabirimide C and imaged over 10 minutes at 10-second intervals. (a) $D_c$ and $D_s$ are depicted as a function of time for both cells. "Coefficients of variance" (standard deviation over the first 200 seconds, divided by average staining intensity) are shown for $D_c$ and $D_s$ traces. (b) $D_{cs}$ in individual cells is shown to correlate with aspect ratio *S*, as predicted by the model and illustrated by the population data in Fig. 3. Each point represents a measurement of the cells shown in panel (a) at a specific time; solid lines are linear fits to the data points. The dashed line shows the predicted relation between $D_{cs}$ and S.

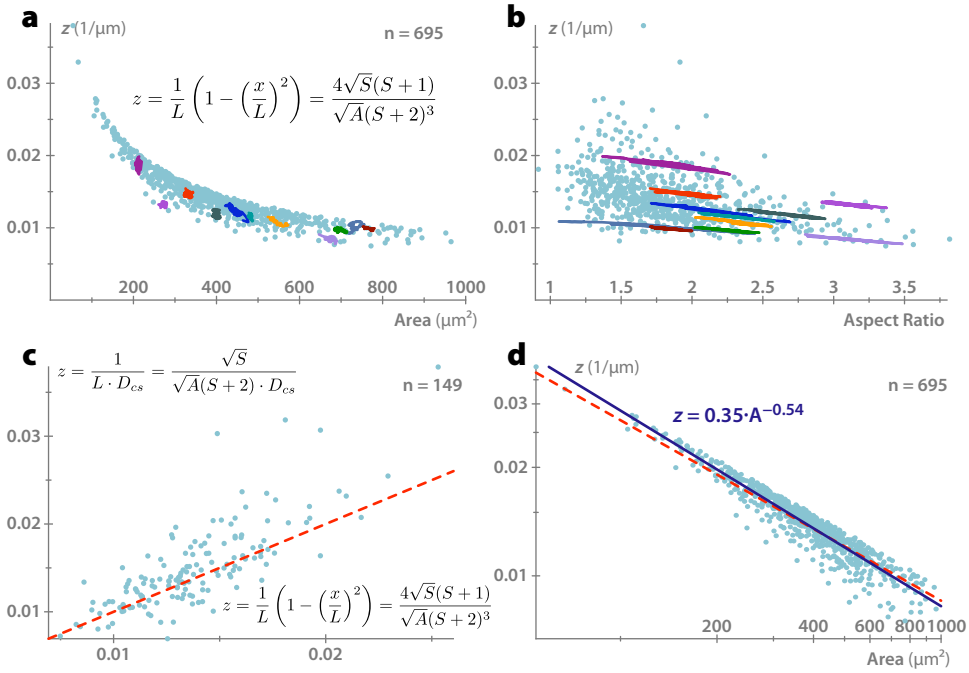


**Figure S5 – Scaling of the model parameter *z* with cell area and aspect ratio.** (a and b) According to the model, the cell-specific parameter *z* can be calculated as a function of cell area A and aspect ratio S. Here, z(A, S) is plotted versus *A* (a) and *S* (b). Each blue circle depicts data from a single cell in the population data set. The colored lines represent data from measurements of eleven individual cells taken at 10s interval over a total of 10 minutes (each color depicts a different cell). Together, (a) and (b) demonstrate that the z-values for the population of cells lie relatively homogeneously within a small range of possible z-values, and that for a given cell over time, z remains largely constant. (c) z-values calculated as a function of cell area and aspect ratio (as in the previous panels) are plotted against z-values as calculated from area, aspect ratio, and the observed actin center-to-sides ratio $D_{cs}$. For reference, z=z is plotted in red. (d) log(*z*) is plotted as a function log(*A*) for the population data. The solid line depicts the best linear fit to the log-transformed data, suggesting that the model parameter *z* scales with cell area as $z \propto A^{-0.54}$, which is consistent with the observation that cell area is slightly correlated with aspect ratio in the population (see Fig. S2 as well). For comparison, the dashed line represents the best fit to the data with the exponent of A fixed at −0.5.

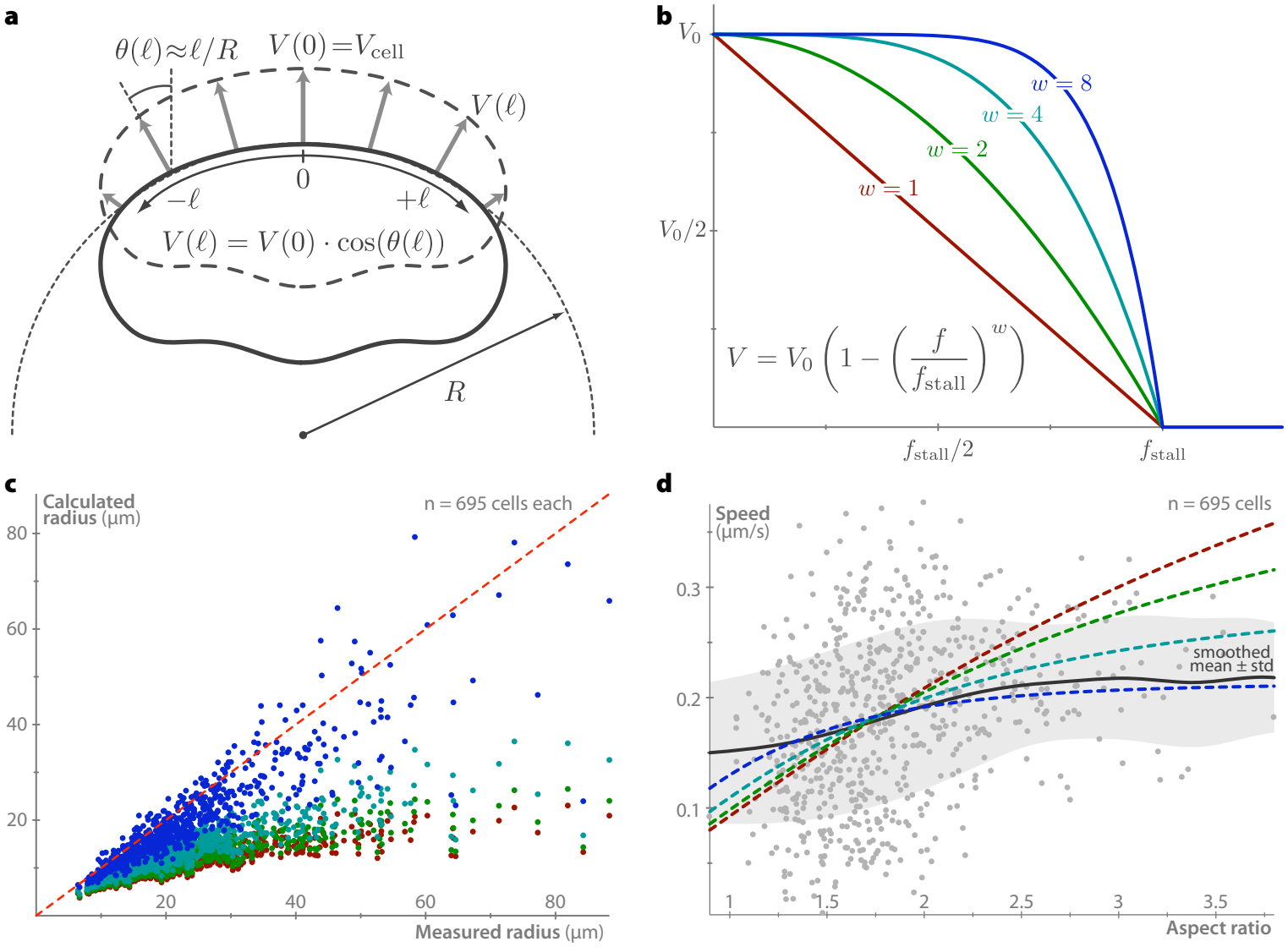


**Figure S6 – Force–velocity relation links graded actin distribution along the leading edge to cell speed and lamellipodial radius.**

(a) Schematic illustration of the graded extension model; cell protrusion is fastest at the cell midline and decreases toward the sides. Cell speed is equal to the maximal protrusion rate at the midline: $V_{cell} = V(0)$. The lamellipodial radius can be calculated using the graded actin distribution, the force–velocity relation and geometrical formulae from the radial extension model. (b) Possible force–velocity relation for a protruding actin network. The polymerization rate, $V$, is plotted as a function of the force per filament, $f$, for $w = 1,2,4,8$. (c) The measured radii of curvature are compared to those calculated using the different force–velocity relations shown in (b). (d) Cell speed is depicted as a function of aspect ratio. Dashed lines indicate the model predictions for this relationship using the different force–velocity equations shown in (b). Dots represent measured values from a population of live cells, with the Gaussian-weighted moving average (σ=0.25) ± one standard deviation shown by the solid line and shaded region (as in Fig. 4b).

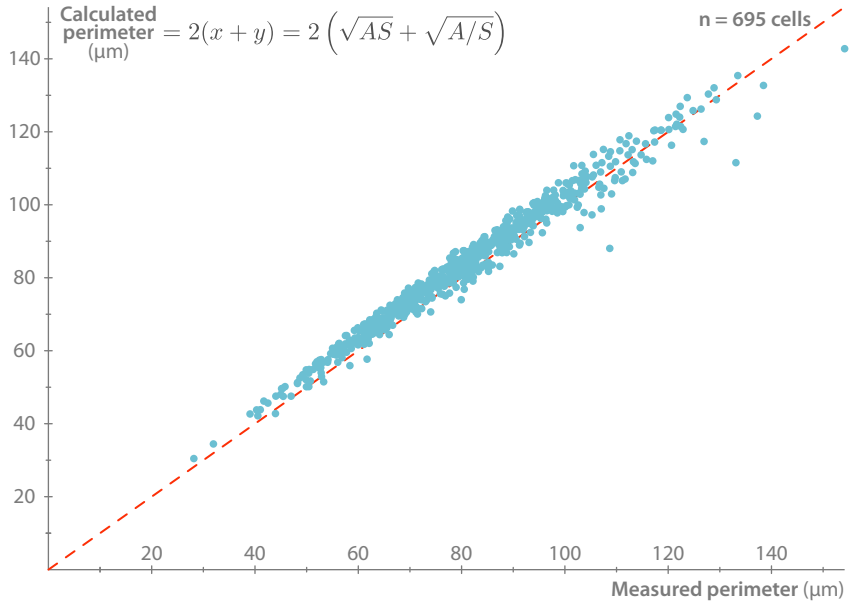


**Figure S7 – The rectangle assumption approximates cell perimeter well.** The calculated cell perimeter based on the measured cell area, *A*, and aspect ratio, *S*, using the rectangle approximation is plotted as a function of the measured perimeter. The close fit indicates that the rectangle assumption gives a good approximation of cell shape.

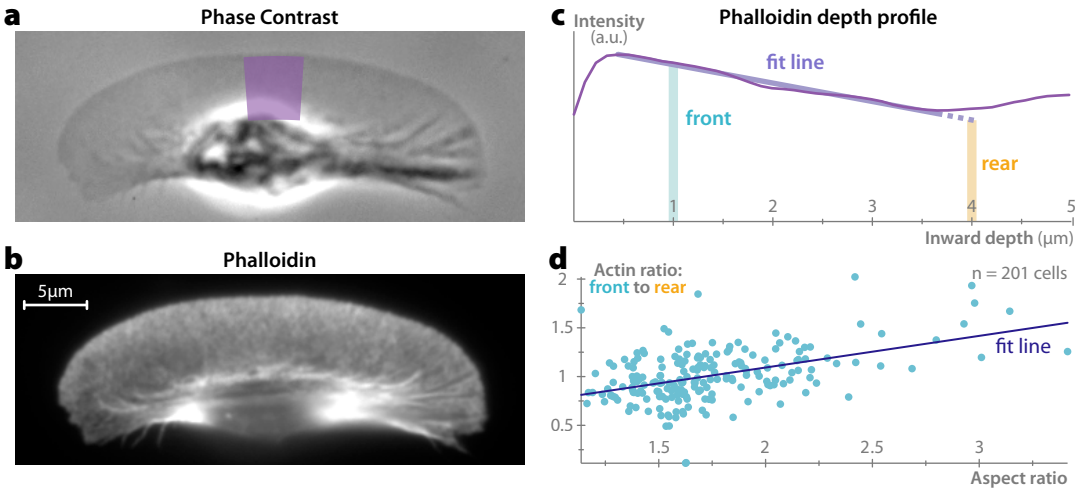


**Figure S8 – Front-to-rear slope in actin filament density correlates with cell aspect ratio.** Phase-contrast (a) and fluorescence (b) images of a fixed cell stained with TRITC-phalloidin. (c) The profile of the (background-subtracted) fluorescence intensity of that cell is shown as a function of distance from the leading edge. The profile was averaged along the width of the region highlighted in (a). The measured profile was fit in the indicated region (solid line; fitting region is bounded per-cell by the maximum intensity within the first μm of depth and the minimum intensity beyond 3.5 μm) and the front-to-rear ratio (the ratio of the height of the fit line at 1 and 4 μm from the leading edge) was used as a measure of the slope. (d) The front-to-rear ratio is plotted against the cell aspect ratio. Each data point corresponds to an individual cell.

as extrinsic ubiquitin receptors of the proteasome[5,7]. Thus, the question of ubiquitin receptors seemed to be answered. As we now find out, however, the 26S proteasome concealed an additional intrinsic ubiquitin receptor.

In the first of the new papers, Husnjak *et al.*[1] describe how they have identified human Rpn13, a regulatory-particle subunit, as a ubiquitin-binding protein. Although both the amino- and carboxy-terminal regions of Rpn13 are conserved among species, the ubiquitin-binding activity is located at what is known as a pleckstrin-homology-like domain at the amino terminus (pleckstrin-homology domains are common in proteins involved in intracellular signalling). Rpn13 from budding yeast has only the amino-terminal conserved domain.

Husnjak *et al.*[1] first addressed the significance of the ubiquitin-binding activity of Rpn13 in purified 26S proteasomes. Although proteasomes lacking all known ubiquitin-receptor activities — including the UIM of Rpn10 and three UBL–UBA-containing proteins — still bound to the polyubiquitinated substrate, additional deletion of Rpn13 resulted in almost total loss of ubiquitin-binding activity. The defect was restored by either Rpn10 or Rpn13. These results clearly suggest that Rpn10 and Rpn13 are the primary ubiquitin receptors of the 26S proteasome (Fig. 1).

The amino-terminal domain of Rpn13 shows no similarity to known ubiquitin-binding motifs. As Husnjak *et al.*[1] and Schreiner *et al.*[2] recount, the next phase of the research was to use nuclear magnetic resonance and crystallographic studies to determine how Rpn13 binds ubiquitin. These structural analyses revealed that the amino-terminal domain has a canonical pleckstrin-homology fold consisting, in technical terms, of a seven-stranded β-sandwich structure capped by the carboxy-terminal α-helix. The authors therefore named this domain 'pleckstrin-like receptor for ubiquitin' (Pru).

They found that the Pru domain of human Rpn13 shows high affinity (around 90 nanomolar) for diubiquitin, the strongest binding among the known ubiquitin receptors. Both human and yeast Rpn13 Pru domains use three loops at one edge of their β-sheet to bind ubiquitin. The authors successfully created an *rpn13* mutant (called *rpn13–KKD*) that lost ubiquitin-binding capacity without compromising proteasome integrity, and tested the biological effects of this mutation in yeast. Degradation of a model substrate protein of the ubiquitin–proteasome system was retarded in this mutant; and when combined with an *rpn10–uim* mutant, the cells showed further impairment of proteasome function. In addition, polyubiquitinated proteins accumulated in the *rpn10–uim, rpn13–KKD* mutant cells. These results suggest that Rpn13 is a true intrinsic ubiquitin receptor of the 26S proteasome, and that it collaborates with Rpn10 *in vivo*.

An obvious question that arises is why there are so many ubiquitin receptors in the ubiquitin–proteasome system. The 26S proteasome binds with high affinity to the longer polyubiquitin chains, so it is likely that both Rpn13 and Rpn10 can bind simultaneously to a substrate that bears such chains. Rpn13 Pru can also recognize UBL–UBA-containing proteins[1,2], as mammalian Rpn10 does[4]. Perhaps polyubiquitin recognition at multiple sites in the proteasome enhances targeting potency and stabilizes the proteasome–substrate complex for substrate degradation. Intriguingly, yeast cells with mutations in five ubiquitin receptors are still viable, indicating that there may still be unidentified ubiquitin receptors in the proteasome, perhaps operating downstream from Rpn10 and Rpn13. In mammalian cells, Rpn13 binds via its carboxy-terminal domain to Uch37, one of three proteasome-associated deubiquitinating enzymes[8–10]. This means that Rpn13 might be a specialized ubiquitin receptor that can fine-tune the timing of substrate degradation.

More generally, it is becoming apparent that there are several layers to proteasome regulation, and that this may allow the proteasome to cope with high substrate flux as well as a wide diversity of substrates. The identification of Rpn13 as a ubiquitin receptor will help in directing research to elucidate these intricate mechanisms. ■

Yasushi Saeki and Keiji Tanaka are at the Tokyo Metropolitan Institute of Medical Science, 3-18-22 Honkomagome, Bunkyo-ku, Tokyo 113-8613, Japan.
e-mails: saeki@rinshoken.or.jp; tanakak@rinshoken.or.jp

1. Husnjak, K. *et al. Nature* **453,** 481–488 (2008).
2. Schreiner, P. *et al. Nature* **453,** 548–552 (2008).
3. Pickart, C. M. & Cohen, R. E. *Nature Rev. Mol. Cell Biol.* **5,** 177–187 (2004).
4. Deveraux, Q., Ustrell, V., Pickart, C. & Rechsteiner, M. *J. Biol. Chem.* **269,** 7059–7061 (1994).
5. Elsasser, S. & Finley, D. *Nature Cell Biol.* **7,** 742–749 (2005).
6. Wilkinson, C. R. *et al. Nature Cell Biol.* **3,** 939–943 (2001).
7. Verma, R., Oania, R., Graumann, J. & Deshaies, R. J. *Cell* **118,** 99–110 (2004).
8. Yao, T. *et al. Nature Cell Biol.* **8,** 994–1002 (2006).
9. Hamazaki, J. *et al. EMBO J.* **25,** 4524–4536 (2006).
10. Qiu, X. B. *et al. EMBO J.* **25,** 5742–5753 (2006).

BIOPHYSICS

# Cells get in shape for a crawl

Jason M. Haugh

**A cell's shape changes as it moves along a surface. The forward-thinking cytoskeletal elements are all for progress, but the conservative cell membrane keeps them under control by physically opposing their movement.**

The ability of living cells to move affects the way our bodies develop, fight off infections and heal wounds. Moreover, cell migration is an extremely complex process, which explains why it has captured the collective imaginations of a variety of fields, from the biological and the physical sciences. This is good news, because cell motility is determined in equal parts by biochemistry and mechanics[1,2], and so understanding and manipulating it require the sort of clever approach that comes only from the integration of multiple scientific disciplines. On page 475 of this issue, Keren *et al.*[3] combine approaches familiar to cell biology with those familiar to applied mathematics and physics to address how the forces generated by specific molecular processes in a cell produce its observed shape.

The starting point for the authors' analysis was the characterization of variability in the shapes adopted by epithelial keratocytes from fish skin in culture. These cells serve as a unique model system for studying cell migration, because they crawl rapidly and without frequent changes in direction, and maintain a nearly constant shape as they move. Their stereotypical shape, often described as an 'inverted canoe', is characterized by a broad membrane structure at its front, the lamellipodium, which protrudes forward in concert with forces that act at the rear of the cell. The authors determined that most of the shape variability could be attributed to differences in cell size and, to a lesser extent, the aspect ratio of its characteristic dimensions (the ratio of its width to its height).

The key insight by Keren *et al.* was to relate two independent observations: the cell's shape and its distribution of actin filaments. Actin filaments are structural elements inside the cell that, through the energy-intensive process of adding (and later removing) protein subunits, produce the mechanical work required to push the cell forward. New, growing filaments are formed by the branching off of existing ones, a process that is well understood in keratocytes[4,5].

Building on previous work[6], the authors propose a mathematical model to explain the observation that the filament density at the cell front is graded, with the highest density at its centre (Fig. 1). The importance of this approach is that it incorporates known molecular mechanisms, and hence the model could be used to predict what might happen if the functions of the molecules involved were perturbed. The authors next invoked what is known as the force–velocity relationship, which states that the rate at which the

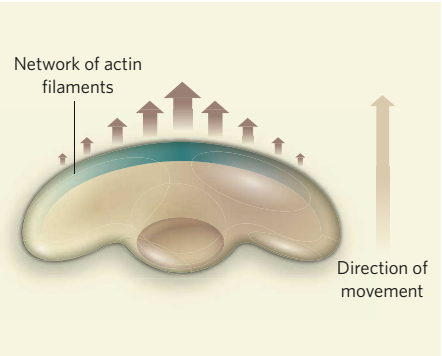


**Figure 1 | Shape matters.** Viewed from above, the characteristic shape of fish keratocyte cells crawling on a surface resembles an inverted canoe. The driving force of the cell's movement comes from actin filaments that form a network at the cell front. The filaments grow in the direction of motion, generating a thrust that overcomes tension in the cell membrane. Keren *et al.*[3] show that the density of actin filaments varies across the cell front (higher-density regions are shown in deeper turquoise). The authors propose that high-density regions generate more thrust than low-density regions (arrow sizes indicate magnitude of thrust). High-density regions thus protrude forward more than low-density areas. This model explains the shapes formed by moving cells.

membrane can be pushed forward by the growing actin filaments decreases as the force resisting them increases, and above a critical value — the stall force — protrusion stops completely.

Although the mechanisms that give rise to this relationship are actively debated, it is strongly grounded by empirical observations[7]. Keren *et al.*[3] reasoned that the load force per actin filament must increase as the filament density decreases from the centre of the cell, and thus the 'sides' of the cell represent the regions of the lamellipodium where the actin filaments are stalled (and/or buckled under pressure; Fig. 1). A specific prediction followed, which the authors confirmed: the steepness of the actin-filament gradient from the cell centre to the front edges is directly related to the cell's aspect ratio. Furthermore, with the specification of the cell shape and the force–velocity relationship, Keren *et al.* showed that they could predict, in a consistent way, the curvature of the cell front and the cell-migration speed.

The elegance of the authors' model, which exemplifies the combined use of quantitative cell biology and mathematical analysis[8], lies in its ability to relate molecular and physical processes with very few or in some cases no adjustable parameters. One unresolved issue that warrants further study concerns the mechanistic implications for the variability in cell size. Although Keren *et al.* were not able to address this point directly, their model suggests that it ought to affect either the rate of actin-filament branching or the tension of the cell membrane, or possibly both. ■

Jason M. Haugh is in the Department of Chemical and Biomolecular Engineering, North Carolina State University, Raleigh, North Carolina 27695-7905, USA.
e-mail: jason_haugh@ncsu.edu

1. Lauffenburger, D. A. & Horwitz, A. F. *Cell* **84,** 359–369 (1996).
2. Ridley, A. J. *et al. Science* **302,** 1704–1709 (2003).
3. Keren, K. *et al. Nature* **453,** 475–480 (2008).
4. Pollard, T. D., Blanchoin, L. & Mullins, R. D. *Annu. Rev. Biophys. Biomol. Struct.* **29,** 545–576 (2000).
5. Pollard, T. D. & Borisy, G. G. *Cell* **112,** 453–465 (2003).
6. Lacayo, C. I. *et al. PLoS Biol.* **5,** e233 (2007).
7. Mogilner, A. *Curr. Opin. Cell Biol.* **18,** 32–39 (2006).
8. Mogilner, A., Wollman, R. & Marshall, W. F. *Dev. Cell* **11,** 279–287 (2006).

ASTRONOMY

# Supernova bursts onto the scene

Roger Chevalier

**The stellar explosions known as supernovae are spectacular but common cosmic events. A satellite telescope's chance observation of a burst of X-ray light might be the first record of a supernova's earliest minutes.**

Once the processes of nuclear fusion that have bolstered it against its own gravity are exhausted, the core of a massive star collapses in on itself. The result is a cataclysmic explosion that sends a violent shock wave racing outwards. As this shock wave reaches the star's surface, it produces a short, sharp burst of X-ray or ultraviolet radiation, the prelude to the expulsion of most of the star's matter into the surrounding medium. Lasting days to months, we see this aftermath of the explosion as a supernova.

That is the theory, at any rate. But although supernovae themselves are common enough, the chain of events that lead up to them — in particular, the exact moment of 'shock break-out' — had never been seen. That all changes with a report from Soderberg *et al.* (page 469)[1]. They observed an intense, but short-lived, X-ray outburst from the same point in the sky where shortly afterwards a supernova flared up, and have thus provided valuable support for the prevalent theories of supernova progenitors.

The authors' discovery was serendipitous: they just happened to be examining the aftermath of a similar supernova, of 'type Ibc', in the same galaxy. The instrument they were using, NASA's Swift satellite, was primarily intended to pinpoint the mysterious flashes of intense, high-energy light known as γ-ray bursts. But, while pursuing this successful main career, the telescope has also developed a useful sideline in X-ray and optical follow-up observations of supernovae.

What Swift spotted[1] was an X-ray outburst that lasted for some 10 minutes. Its energy content was around $10^{39}$ joules, about a hundred-thousandth of the energy expelled in the explosive motions of a supernova. Continued observation of the position of the outburst showed the emergence of a spectrum and an evolution of emission intensity over time typical of a type-Ibc supernova, albeit with a slightly fainter peak luminosity than normal.

The exploding object was also detected by NASA's Chandra X-ray observatory 10 days after the X-ray outburst, as well as in a series of radio measurements between 3 and 70 days after. Similar observations characterize type-Ibc supernovae, and are thought to relate to interaction of the expanding supernova with mass lost from its progenitor before the explosion, which encircles the star as a surrounding 'wind' (Fig. 1). The interaction generates shock waves that accelerate electrons to almost light speed. These electrons in turn emit radio-frequency synchrotron radiation as their paths curve in the ambient magnetic field, and scatter photons from the visible surface of the star, the photosphere, up to X-ray energies.

Taken together, these observations seem to add up to the identification of the X-ray outburst with the supernova — now designated SN 2008D — that followed. One caveat is that, although the energy of the outburst was close to predictions for the shock break-out of a type-Ibc supernova[2], its duration was much longer than expected. The length of the burst should be determined by the time light needs to cross the supernova progenitor, which is 10 seconds or less. The implication, therefore, is that the photosphere of the progenitor star extends farther than expected, perhaps because it has shed a large amount of material before the supernova occurs.

Within the star, the energy behind the shock wave emanating from the core's collapse is dominated by radiation. Outside, it is dominated by gas energy. Shock break-out occurs at the transition between these two modes, when the radiation behind the internal shock wave spreads out into the circumstellar medium and accelerates its gas. As the inner, already accelerated layers of gas catch up with outer, slower-moving layers, an external gas shock wave develops. Soderberg *et al.*[1] suggest that the observed spectrum of the X-ray burst is determined by the shock acceleration of photons from the supernova photosphere. Detailed